Tortuosity in electrochemical devices – A review of calculation approaches

Bernhard Tjaden[1], Dan J. L. Brett[1], Paul R. Shearing[1*]

[1]*Electrochemical Innovation Lab, Department of Chemical Engineering, University College London, WC1E 7JE, UK*
**Corresponding author: e-mail: p.shearing@ucl.ac.uk*

Abstract

The tortuosity of a structure plays a vital role in the transport of mass and charge in electrochemical devices. Concentration polarisation losses at high current densities are caused by mass transport limitations and are thus a function of microstructural characteristics. As tortuosity is notoriously difficult to ascertain, a wide and diverse range of methods has been developed to extract the tortuosity of a structure. These methods differ significantly in terms of calculation approach and data preparation techniques. Here, we review tortuosity calculation procedures applied in the field of electrochemical devices to better understand the resulting values presented in the literature. Visible differences between calculation methods are observed, especially when using porosity-tortuosity relationships and when comparing geometric and flux based tortuosity calculation approaches.

Keywords

Tortuosity; microstructure; diffusion; tomography; modelling

Nomenclature

Parameters

A	Area
B_O	Viscous flow parameter
c	Mole concentration
d	Thickness
D^{eff}	Effective diffusion coefficient
D_i^{eff}	Effective diffusion coefficient of a species
D^{bulk}	Bulk diffusion coefficient
$D_{i,K}$	Knudsen diffusion coefficient
D_{ij}^{eff}	Binary diffusion coefficient
$e_{\alpha_{PDF}}^{i}$	Speed of a species in the particle distribution function
F	Faraday constant
$f_{\alpha_{PDF}}^{i}$	Particle distribution function
i	Current density
i_{lim}	Limiting current density
J_{eff}	Effective diffusion flux
M	Molar mass

n	Equivalent electrons per mole of reactant
$\dot{n}_{fuel}$	Molar flow rate of fuel gas
N_M	MacMullin number
p	Pressure
p^0_{fuel}	Partial pressure of fuel at the gas inlet
$\dot{q}_{eff}$	Effective heat flux
R	Ideal gas constant
$\langle r^2(t) \rangle$	Mean square displacement
r_P	Mean pore radius
T	Temperature
t	Time
V_{phase}	Volume fraction of analysed phase
w	Mass fraction
x	Mole fraction
x_{PDF}	Location of a species in the particle distribution function

Symbols

α	Bruggeman exponent
α_{PDF}	Direction of movement of a species in the particle distribution function
γ	Scaling factor
δ	Constrictivity
ε	Porosity
$\frac{\varepsilon}{\tau^2}$	Diffusibility or effective relative diffusivity
κ	Tortuosity factor
κ_{geo}	Geometric based characteristic tortuosity factors
κ_{geo}	Flux based characteristic tortuosity factors
λ^{bulk}	Bulk thermal conductivity
μ	Dynamic viscosity
σ^{bulk}	Bulk conductivity
σ^{eff}	Effective conductivity
τ	Tortuosity
τ_C	Characteristic tortuosity
$\Omega^i_{\alpha_{PDF}}$	Collision term of a species in the particle distribution function

1. Introduction

Electrochemical devices, including fuel cells and batteries, will play an increasing role in our live, particularly as we transition to a low-carbon economy. However, in order to accelerate their commercialization across a range of applications, an improved understanding of the underlying material characteristics is required. The importance of the effect of microstructure on the performance of electrochemical devices has been widely demonstrated[1], which is why studies of microstructural analysis techniques[2] are crucial for optimizing vital parameters. Among these parameters, tortuosity plays an essential role in mass transport and concentration polarisation resistance.[3] Yet, calculating the tortuosity is not trivial, which is why a wealth of tortuosity

calculation methods has been developed, not only in the electrochemical community, but across many fields of research (optics, magnetism, geology, medicine, etc.), each with associated definitions and areas of application.[4,5]

The microstructure of porous electrode and support layers in electrochemical devices is the main contributor to performance losses, especially in mass transport limiting operating regimes. This is valid for batteries, fuel cells and oxygen transport membranes alike, where tortuosity is used to relate the effective transport properties of diffusion and electric or ionic flux, to its respective bulk property. As such, tortuosity is an indispensable parameter in modelling and quantifying fuel cell[6] and battery behaviour.[7] In addition, tortuosity serves as an input parameter in Newman-type models of battery performance[8] and the Adler-Lane-Steele model for electrode kinetics.[9]

Due to the importance of tortuosity for electrochemical devices, and the multitude of calculation approaches, this article reviews the use of tortuosity and various tortuosity calculation methods in the field of electrochemistry. These methods can differ considerably from each other in terms of calculation approach and data preparation techniques. Here, we deal with each in turn.

2. Definition of Tortuosity

In geometrical terms, tortuosity τ is defined as the fraction of the shortest pathway through a porous structure Δl and the Euclidean distance between the starting and end point of that pathway Δx, illustrated in Figure 1. As such, τ always amounts to a value equal to or greater than unity. In general, when analysing a porous structure, there exists only one shortest pathway and one tortuosity value. From this geometric perspective, constrictions or bottlenecks of the pore structure are not considered. The concept of tortuosity has been adopted in a variety of sciences[4,5] such as gaseous mass transport and electronic and ionic conductivity through porous, functional layers. In these fields, tortuosity is applied in a broader way than just a simple geometric measure of the shortest path length; tortuosity is also used to quantify and describe the resistance of a structure to a flux. In this respect, the difference between “tortuosity” and “tortuosity factor” was coined by Epstein in 1989,[10] who used a capillary model to show that the tortuosity τ is the square root of the tortuosity factor κ, as presented in Eq. (1).

The tortuosity factor accounts for both the additional path length and its change in velocity of a species when migrating through a porous structure. Epstein then applied this derivation in the field of diffusion, where the tortuosity factor is used to calculate the effective diffusion coefficient D^{eff} based on the bulk diffusion coefficient D^{bulk}, shown in Eq. (2), which is also valid for ionic and electronic conductivities. The nomenclature distinguishing between κ and τ is adopted in this review and values are converted accordingly, where necessary.

$$\kappa = \tau^2 \qquad \text{Eq. (1)}$$

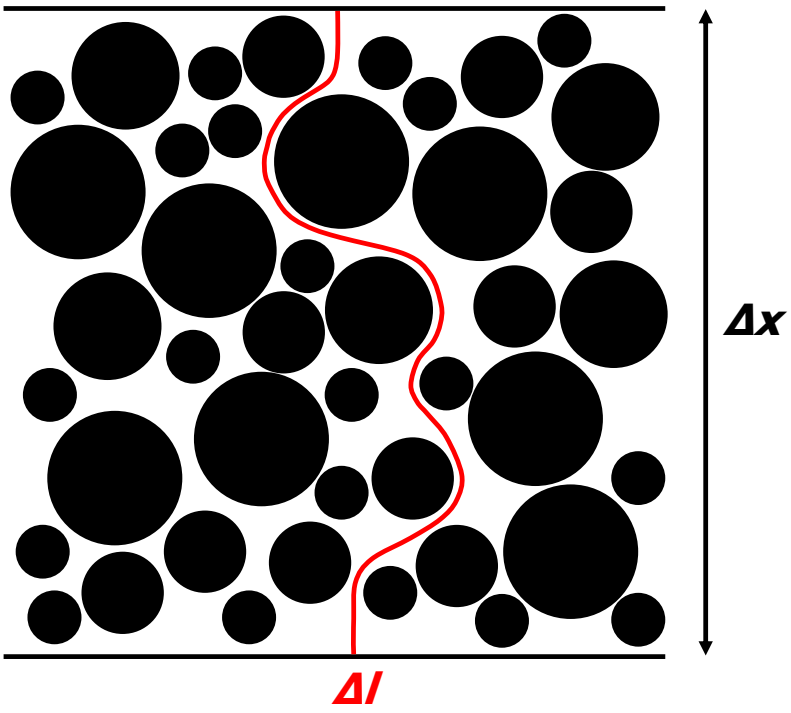

Figure 1: Representation of the geometric definition of tortuosity, which is the fraction between the shortest path through a porous structure Δl and the Euclidean distance between the starting and endpoint of that pathway Δx

$$D^{eff} = \frac{\varepsilon}{\kappa} D^{bulk} = \frac{\varepsilon}{\tau^2} D^{bulk} \quad \text{Eq. (2)}$$

$$D^{eff} = \frac{\varepsilon\,\delta}{\tau} D^{bulk} \quad \text{Eq. (3)}$$

Yet, the theory behind the tortuosity factor, is controversial, especially in the field of diffusive mass transport: van Brakel and Heertjes[11], for example, defined a constrictivity factor δ to account for the variation in pore diameter along the diffusion pathway, which is included in calculating the effective transport property via Eq. (3).

This constrictivity factor was later adopted by Holzer *et al.*[12] who stated that the implementation of τ^2 was used to explain high values of experimentally derived tortuosities. Consequently, the authors differentiated between two types of tortuosity:[12,13]

1. That, which is acquired by indirect calculations based on experimental data τ_{exp}.
2. And that, which is determined via geometric algorithms from reconstructed 3D volumes τ_{geo}.

Additionally, when analysing diffusive mass transport problems, depending on the diffusion mechanism taking place through a porous medium (ordinary, Knudsen and/or viscous diffusion)[14] and on the gases involved[15], different tortuosity values may dominate.

The geometric definition of tortuosity clearly suggests that there exists only one shortest pathway through a porous membrane. Yet, this pathway might not be the predominant diffusion pathway of gases and does not account for constrictive pores; not all molecules will be affected by the microstructure to the same extent when migrating through such a layer. The inherent difference of the mean free path between each gaseous species leads to different Knudsen numbers and thus, different diffusion pathways for different species at different temperatures, gas compositions and

transport regimes. It can thus be inferred, that for each species and each transport regime, a different tortuosity value is dominating.

Moreover, in experimental approaches, tortuosity is not always presented explicitly, but is rather combined with porosity into a "diffusibility"[16,17] or "effective relative diffusivity"[18,19] value expressed as $\frac{\varepsilon}{\tau^2}$. Additionally, in the field of battery research, tortuosity is contained in the MacMullin number N_M, which relates the bulk conductivity of the electrolyte σ^{bulk} to the effective conductivity of the porous electrolyte σ^{eff}:[20–23]

$$N_M = \frac{\sigma^{bulk}}{\sigma^{eff}} = \frac{\tau^2}{\varepsilon} \qquad \text{Eq. (4)}$$

The different definitions and applications of the term tortuosity, *i.e.* the differentiation between geometric and flux/conductivity based tortuosity, entail differences in their significance, interpretation and calculation approach. This is reflected by the vast number of tortuosity calculation approaches shown here.

3. Porosity-Tortuosity Relationships

Employing a porosity-tortuosity relationship is one of the most fundamental and straightforward approaches to derive a tortuosity (or effective medium property) of a porous structure. Such relationships, of theoretical or empirical origin, directly calculate a tortuosity value solely based on a porosity of a sample.

In the comprehensive work by Shen and Chen,[24] a review of past and present correlations is provided, among which the Bruggeman equation is the most well-known and most widespread relation in the field of electrochemistry.[25] Eq. (5) presents the generally used form of the Bruggeman relationship, where α is the Bruggeman exponent which, in its standard form, is considered to be 1.5. Recently, the authors have provided a translation and explanation of the mathematical formulation of Bruggeman which is used to derive the widely used model.[26]

$$\tau^2_{Bruggeman} = \varepsilon^{1-\alpha} \qquad \text{Eq. (5)}$$

Whilst the history of the Bruggeman correlation can be traced back to the 1930s, its proliferation is not notable until the 1950s: Hoogschagen was one of the first to use the Bruggeman and Maxwell relation (*cf.* Eq. (6)) to validate experiments, where gas diffusion through glass spheres was measured. He observed, that values for the labyrinth factor ($\frac{1}{\tau^2}$) lay between the Maxwell and Bruggeman correlation, but slightly closer to the latter.[16]

$$\tau^2_{Maxwell} = \left(\frac{3-\varepsilon}{2}\right) \qquad \text{Eq. (6)}$$

De La Rue and Tobias achieved similar results when measuring the effective conductivity values of liquid $ZnBr_2$ electrolyte solution. A variety of non-conducting glass spheres of different sizes were embedded into the electrolyte to achieve different volume fractions. The conductivity as a function of volume fraction of the embedded phase was evaluated. As was the case in Hoogschagen's publication,[16] results lay between the Maxwell[27,28] and Bruggeman relation.[29] Since then, the Bruggeman equation has become a commonly used method to derive effective medium properties

of porous structures in batteries[30–34] and proton exchange membrane (PEM) fuel cells.[35–44] Moreover, it has been implemented as a standard addition to predicting microstructures in electrochemistry models, such as in the COMSOL Multiphysics modelling software (COMSOL, Inc.).[23]

However, predictions given by the Bruggeman correlation are not always consistent with experimental results.[23,45] As a consequence, researchers have adjusted the Bruggeman equation by altering the exponent α to fit experimental values. Thorat *et al.* [46] even included an additional scaling factor γ to correlate the Bruggeman model with their experiments, resulting in Eq. (5) to be extended to the following form:

$$\tau^2_{Bruggeman} = \gamma\, \varepsilon^{1-\alpha} \qquad \text{Eq. (7)}$$

Thorat *et al*. used AC impedance spectroscopy and the polarization-interrupt method (*cf*. section 4.2) to extract the tortuosity of a battery separator (Celgard 2400) and cathode samples ($LiFePO_4$ and $LiCoO_2$). Tortuosity values of the battery cathode samples were plotted as a function of porosity and an exponential fitting curve was superimposed. The exponent of the fitting curve amounted to -0.53, which is equivalent to a Bruggeman exponent of 1.53 and thus, very close to its derived value. However, achieved tortuosities were almost twice as high as predicted by the standard Bruggeman relationship, which is why a scaling parameter γ amounting to 1.8 was introduced. This approach of adjusting α and γ was widely adopted showing, that depending on the analysed structure, both parameters can deviate visibly from the ideal values of 1 and 1.5, respectively.[31,46–54]

A further refinement of this approach was realised by Zacharias *et al.*,[52] who made α and γ a function of their battery electrode composition. For this, the dry weight fraction of graphite, carbon black and polyvinylidene fluoride were considered, resulting in higher γ values (2.5 and 2.6) and lower α values (1.27 and 1.28) compared to values from Thorat *et al*.[46]

Table 1 and Figure 2 compare several derived Bruggeman exponents and scaling parameters for different porous materials for battery applications. These were each extracted as a function of several experimental measurement points and used to extrapolate the presented curves as function of porosity. It is notable, that even for this small class of materials, values for α and γ differ significantly from each other. The differences in manufacturing techniques, and also the differences of composition, pore size distribution and other microstructural characteristics of each battery layer contribute to such a large spread of values. Some of these derivations, however, achieve tortuosity values below unity when extrapolated to high porosity values, which is in contradiction to the definition and physical significance of τ. Moreover, a porosity of one necessitates a tortuosity of one. Yet, this is not achieved by all correlations. Both of these findings cast doubts on the usefulness of this method. As a consequence, the application and interpretation of α and γ values have to be analysed with caution.

Hence, evaluating the validity of the Bruggeman correlation is still an ongoing field of research. Chung *et al.*[55] used X-ray computed tomography and simulation techniques for an extensive study to evaluate the effect of battery membrane fabrication and processing methods on the tortuosity. In total, 16 $LiNi_{1/3}Mn_{1/3}Co_{1/3}O_2$ battery electrodes with varying weight ratios were manufactured and reconstructed using X-ray synchrotron tomography.[56] Tortuosity was then extracted by simulating mass transport according to Fick's law across the sample volume (see section 5.2). It was shown, that calculated tortuosity values always lie slightly above the Bruggeman correlation. For further investigation, samples based on the particle size distributions of the imaged samples were computer generated, for which the orientation and particle packing was varied. It was discovered, that

perfectly ordered particle distributions result in tortuosities close to the Bruggeman relationship throughout the range of porosity values.[55]

Continuing work in the field of battery research from Wood and co-workers (*cf*.[53,55,56]) culminated in the development of an open source program called *BruggemanEstimator*.[57] This program allows the extraction of the Bruggeman exponent α in each dimension of a 3D sample volume by using two 2D images, namely one top view and one cross-sectional view. The Bruggeman exponent of the sample is achieved by applying the differential effective medium approximation method introduced by Bruggeman. In comparison to previously obtained values, results calculated by the *BruggemanEstimator* software agreed well with numerical tortuosity calculation methods[57] and has been recently applied in practice.[58] This approach is similar to stereological methods which quantify 3D properties based in 2D image slices.[59] The advantage of stereology is the reduced experimental efforts necessary to extract results. However, Taiwo *et al*.[2] recently concluded, that values based on stereological approaches may deviate visibly from 3D measurements.

Table 1: Comparison of Bruggeman exponent and scaling parameter for battery layers fitted to experimental results

Material	γ	α	Reference
Battery electrode	1	3.3	Doyle *et al*.[47]
Battery electrolyte	1	4.5	Doyle *et al*.[47]
Battery separator	1	2.4	Arora *et al*.[31]
Battery electrode	1	5.2	Arora *et al*.[31]
Battery electrode	1.8	1.53	Thorat *et al*.[46]
Battery electrode	0.115	3.2111	Kehrwald *et al*.[50]
Battery electrode	0.1146	3.159	Kehrwald *et al*.[50]
Battery electrode	2.5	1.27	Zacharias *et al*.[52]
Battery electrode	2.6	1.28	Zacharias *et al*.[52]
Battery separator	0.667	2.43	Cannarella *et al*.[51]
Battery separator	0.58	3.33	Cannarella *et al*.[51]
Battery separator	1.77	1.77	Cannarella *et al*.[51]

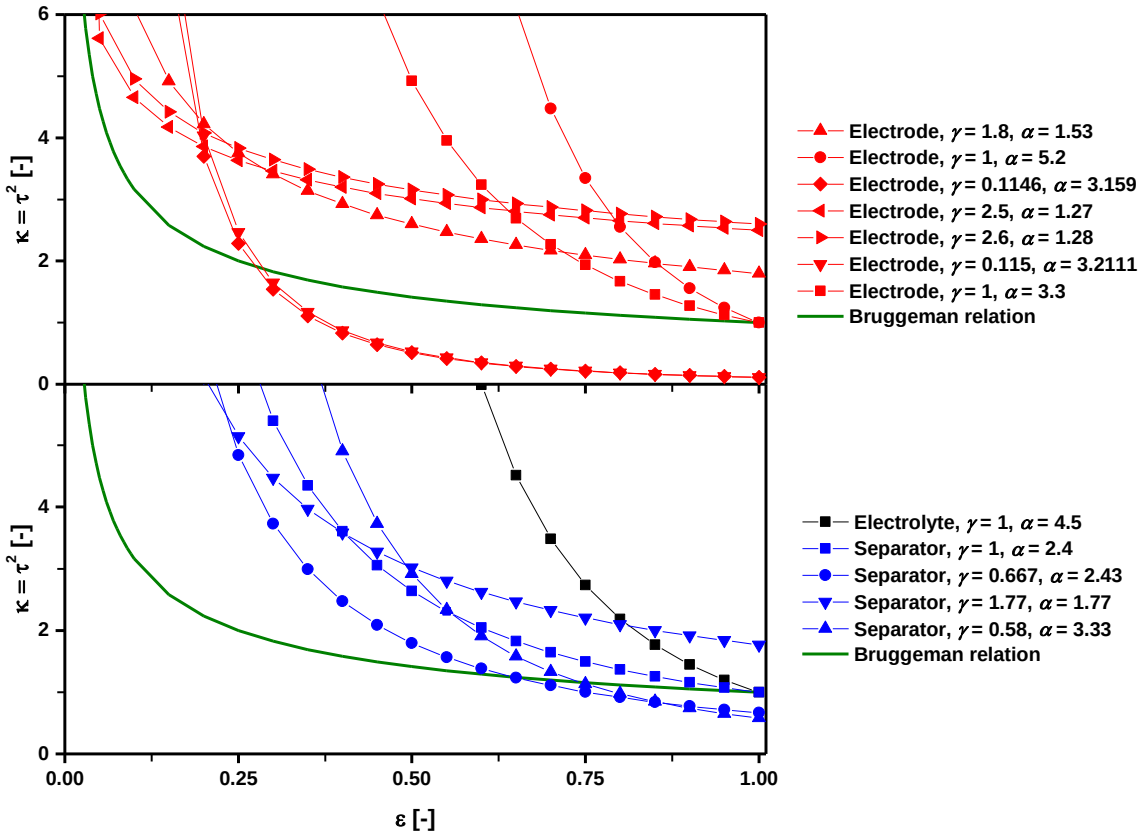

Figure 2: Comparison of Bruggeman exponents and scaling parameters for different battery layers referenced in Table 1

Moreover, a wide range of recent studies report conflicting results on the validity of the Bruggeman correlation when compared to calculations conducted using tomography techniques. Conclusions vary substantially as in some instances, simulations agree well with the Bruggeman correlation,[33,55] while considerable disagreement was observed in other cases.[44,60–62] The reason for this seems to be sample specific, as heterogeneity and geometry are characteristics of porous materials that are not accounted for by the Bruggeman correlation. The aforementioned studies have shown that the characteristic shape of the analysed microstructure has considerable effects on the validity of the Bruggeman relation: spherical structures, which follow Bruggeman's initial hypothesis very closely, adhere to the correlation. The correlation, however, is less suitable for connected solid phases and complex porous networks.

This is further complicated by the distinctions (or lack thereof) between geometrical and transport limiting tortuosity.[63] Moreover, porosity-tortuosity relationships provide limited information in areas, where the analysed sample consists of several layers with different microstructural features Such as multi-layer battery separators[51] which combine different properties into a single separator; *i.e*. each individual layer exhibits distinct structural properties, and for this reason, the simplified assumption of a homogenous sample volume made by the Bruggeman correlation is no longer valid. As a conclusion, it can be stated that porosity-tortuosity relationships are only applicable and reliable when executed across homogeneous microstructures which are similar to the microstructure used to derive the respective relationship.

4. Experimentally Derived Tortuosity

Historically, the lack of detailed geometrical information on complex porous media in 3D has limited the ability of researchers to extract meaningful data on the tortuosity of a porous body. In the absence of this information, effective transport properties of porous structures have been derived experimentally by means of diffusion cell experiments[16,17,64–70]and electrochemical measurements.[15,19,46,71]

4.1. Diffusion Cell Experiments

As reviewed by He *et al*.[72] diffusion measurement methods in the field of fuel cell research aim at extracting effective diffusion coefficients for distinct gas mixtures. Typically, a porous sample is mounted between an upper and a lower gas channel where two different gases enter the upper and lower chamber. Due to the concentration gradient across the porous material, diffusion of either gas to the opposite channel is induced. Measuring the concentration of either gas both streams allows the calculation of the diffusion fluxes across the membrane via a mass balance over the cell, as illustrated in Figure 3. The effective binary diffusion coefficient and in turn, the tortuosity of the sample, are subsequently derived by applying a suitable diffusion model.

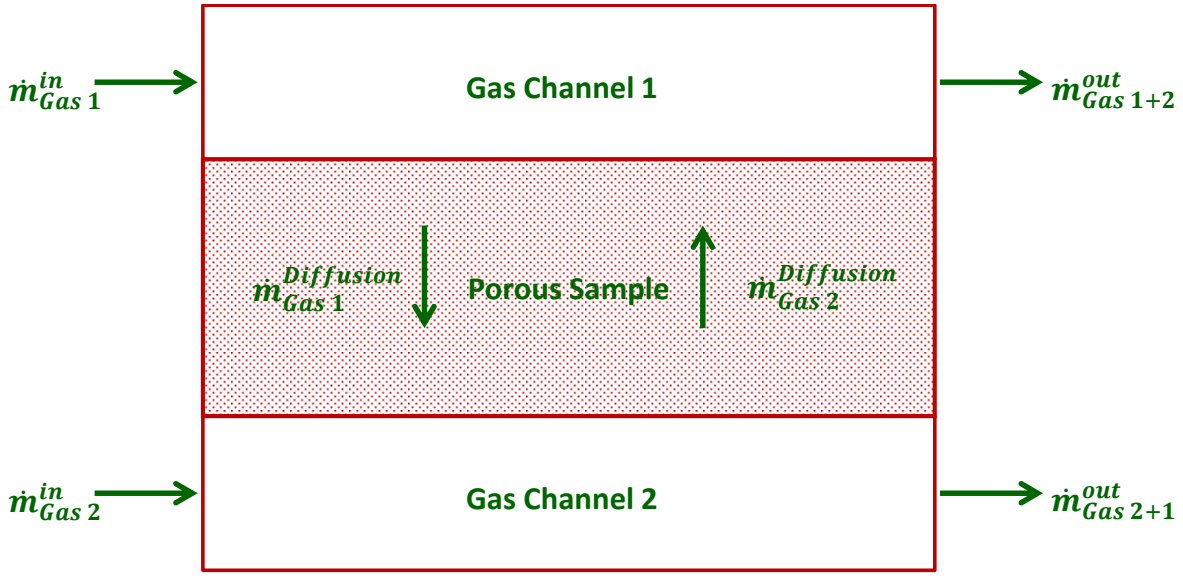

Figure 3: Mass balance over a Wicke Kallenbach diffusion cell to extract the diffusion flow rate across a porous sample

The applicability of such models is dependent on the diffusion mechanism taking place through the porous medium (ordinary, Knudsen and/or viscous diffusion *cf*.[14,73,74]). The most direct diffusion model considering ordinary and Knudsen diffusion is the Fick model. For this, Fick's law is extended by combining the Knudsen diffusion coefficient $D_{i,K}$, (Eq. (8)) with the effective binary diffusion coefficient D_{ij}^{eff} via the Bosanquet equation (Eq. (9)). Moreover, Fick's model is capable of incorporating viscous flux via Darcy's law, as presented by Eq. (10). In this case the model is referred to as advective-diffusion model.[75]

In the following equations, r_P is the mean pore radius, R is the ideal gas constant, T the temperature, M the molar mass, D_i^{eff} is the effective diffusion coefficient of a species, B_O is the viscous flow parameter and μ is the dynamic viscosity and p the pressure and w the mass fraction.

$$D_{i,K} = -\frac{2}{3}\, r_P\, \frac{\varepsilon}{\tau^2} \sqrt{\frac{8\, R\, T}{\pi\, M}} \qquad \text{Eq. (8)}$$

$$D_i^{eff} = \left(\frac{1}{D_{ij}^{eff}} + \frac{1}{D_{i,K}} \right)^{-1} \quad \text{Eq. (9)}$$

$$J_{i,D} = -\frac{1}{R\ T} \left(D_{ij}^{eff}\ \nabla p_i + \frac{B_O\ c_i}{\mu}\ \nabla p \right) \quad \text{Eq. (10)}$$

While Fick's law assumes equimolar diffusion in a binary gas mixture, Mills[76] suggested that diffusion follows equimass principles. By converting the molar concentration gradient of Fick's first law into a gradient of mass fraction, the governing equation for equimass diffusion was achieved:

$$J_{i,D} = -D_i^{eff}\ \frac{p}{R\ T}\ \frac{M_i\ M_j}{\left[w_i \left(M_j - M_i \right) + M_i \right]}\ \nabla w_i \quad \text{Eq. (11)}$$

Again, the Bosanquet equation and Darcy's law can be used to extend the formulation to cater for additional diffusion mechanisms besides ordinary diffusion. The effective diffusion coefficients are directly achieved via the above models which make their application straightforward. More complex models such as the Dusty Gas Model (DGM) [73] or Maxwell-Stefan Model (MSM), shown in Eq. (12) and Eq. (13), respectively, combine several diffusion modes *a priori*. The DGM, for example, includes expressions for ordinary, Knudsen and viscous flux, where *x* is the molar fraction:

$$\frac{J_{i,D}}{D_{i,K}} + \sum_{j=1, j\neq i}^{n} \frac{x_j\ J_{i,D} - x_i\ J_{j,D}}{D_{ij}^{eff}} = -\frac{p\ \nabla x_i}{R\ T} + \frac{x_i\ \nabla p}{R\ T} \left(1 + \frac{B_O\ p}{\mu\ D_{i,K}} \right) \quad \text{Eq. (12)}$$

The MSM uses the same correlation as the DGM, but neglects Knudsen diffusion effects. As a result, coefficients related to Knudsen diffusion drop out of equation Eq. (12) and result in the following formulation:

$$\sum_{j=1, j\neq i}^{n} \frac{x_j\ J_{i,D} - x_i\ J_{j,D}}{D_{ij}^{eff}} = -\frac{p}{R\ T}\ \nabla x_i \quad \text{Eq. (13)}$$

The accuracy of these models has been discussed[77] and evaluated in literature, predominantly by comparing them to measured concentration polarisation losses in SOFC anodes.[78,79] In these experiments, the DGM achieved highest accuracy among the analysed models, which might be one reason for its widespread use in literature,[79–83] while the simplicity but lower accuracy of the Fick model was frequently highlighted. However, in these cases, tortuosity is usually used as a fitting parameter to tailor calculation results to measured data. Consequently, the extracted tortuosity values are highly dependent on the accuracy of the applied model.

One recent application of extracting the tortuosity of a porous sample via diffusion cell experiments was presented by Tjaden *et al*.[84]. In their analysis, a variety of binary gas mixtures were tested on a planar YSZ porous support layer of an oxygen transport membrane. It was shown, that the tortuosity for different binary gas mixtures is not a constant value but depends on the involved gaseous species. Due to the difference in mean free path between the different constituents, different diffusion pathways dominate and thus, different tortuosity values are achieved. For example, at ambient temperature, tortuosity based on the diffusive flux of CH_4 in the CH_4-N_2 binary gas mixture amounted to approximately 2.3 while tortuosity of the N_2 diffusion flux amounted to approximately

2.5. In addition, the authors showed, that tortuosity increased with increasing temperature: the average tortuosity of all binary gas mixtures increased from 2.36 to 2.73.

Contrary temperature dependent behaviour of measured diffusion coefficients was observed by Zamel *et al*.[17] A Loschmidt cell was used to measure the effective diffusion coefficient of a O_2-N_2 gas mixture migrating through carbon paper, which is commonly applied as gas diffusion layer in PEM fuel cells. When increasing the temperature from 25 °C to 80 °C, the bulk diffusion coefficient of the gas mixture, achieved via a resistance network model based on Fick's law, increased from approximately 0.2 cm^2/s to 0.275 cm^2/s while the effective diffusion coefficient increased from approximately 0.05 cm^2/s to 0.075 cm^2/s. This causes the factor $\frac{\varepsilon}{\tau^2}$ to increase by approximately 11.5 % from 0.252 to 0.281. Thus, when considering a constant porosity value, the tortuosity decreases to the same extent. In addition, the authors compared the calculated diffusibility values to a set of porosity-tortuosity relationships, among others, the Bruggeman relation. In all cases, these relationships overestimate the effective diffusion coefficient (and thus, underestimate tortuosity), which was also observed by Tjaden *et al*.[84]

The discrepancies in temperature dependence might be caused by the fundamental difference in microstructural aspects: while YSZ based porous structures are tailored to feature connected solid phases with specific porosities, carbon paper based gas diffusion layers are an accumulation of randomly oriented, fine fibres, typically with much higher porosity. The resulting differences in pore size distribution, mean pore diameter and porosity cause the observed diffusion mechanisms to differ visibly among such samples.

4.2. Electrochemical Experiments

Mass transport limitations play a vital role in electrochemical devices as they are responsible for concentration polarisation at high current densities. For example, as current densities increase, the fuel demand in a fuel cell increases linearly, as shown below, where $\dot{n}_{fuel}$ the molar flow rate of fuel gas, *i* the current density, *A* the area, *n* the equivalent electrons per mole of reactant and *F* the Faraday constant:[6]

$$\dot{n}_{fuel} = \frac{i\,A}{n\,F} \qquad \text{Eq. (14)}$$

The fuel consumption rates at the active sites of a fuel cell are limited by the maximum diffusion rate of fuel through the porous structures. As introduced in previous sections, diffusive mass transport and as such, mass transport limitations, are a function of the complex microstructure of the involved porous membrane layers. Hence, microstructural parameters such as tortuosity are achievable by measuring concentration losses of fuel cells and applying gas diffusion theory.

In this respect, SOFCs offer the possibility to investigate the effect of fuel gas compositions on the performance due to their wide fuel flexibility. A thorough study of on this topic was presented by Jiang and Virkar.[15] As the effects of mass transport limitations are dominating under high current density operations, Jiang and Virkar modified Fick's law to express the effective diffusion coefficient as a function of the limiting current density of the fuel cell under specific operating conditions. The resulting equation is presented thereafter, where i_{lim} is the limiting current density, p^0_{fuel} the partial pressure of fuel at the gas inlet and *d* is the thickness:

$$D^{eff} = \frac{i_{lim}}{\frac{2\,F\,p^0_{fuel}}{R\,T\,d} - \frac{i_{lim}}{R\,T\,\delta}\,\frac{A\,p}{\dot{n}_{fuel}}}$$ Eq. (15)

The limiting current density was measured experimentally from polarisation curves for a set of binary and ternary fuel gas mixtures including H_2-H_2O, CO-CO_2, H_2-He-H_2O, H_2-N_2-H_2O and H_2-CO_2-H_2O, each under varying concentrations. Tortuosity values were then calculated by reversing the Bosanquet equation shown in Eq. (9). At 800 °C, the lowest tortuosity values were achieved for the H_2-H_2O mixture, which, on average, amounted to 2.23, while the highest tortuosity values were calculated for the H_2-CO_2-H_2O mixture, amounting to 2.73. Moreover, in direct comparison between the two binary gas mixtures, it was revealed, that fuel cell performance was higher using H_2 as fuel gas rather than CO which, besides the lower electrochemical activity of CO, was due to the significantly faster diffusion rate of H_2. These results confirm the findings of different tortuosity values for different binary gas mixtures presented in the previous chapter.

Brus *et al*.[71] adopted the same methodology to compare electrochemically derived tortuosity values with an image based tortuosity calculation method, namely the random walk method (*cf*. section 5.2.1). For their experiments, a button-type SOFC sample was manufactured to measure impedance spectra and polarisation characteristics at 700 °C and 800 °C. This way, the limiting current densities were extracted for H_2 concentrations between 2.5 % and 90 % in N_2 and inserted into Jiang and Virkar's model. After these experiments, the 3D microstructure of the anode was reconstructed using FIB-SEM tomography and the random walk method was executed. For each hydrogen concentration and for both operating temperatures, a distinct tortuosity value is calculated whereas the random walk method results only in a single value as shown in Figure 4. Here, only the tortuosity values calculated for low hydrogen concentrations and as such, high concentration polarisation, were considered as accurate representative values. In these cases, the experimentally derived tortuosities agreed well with the random walk value. Hence, under standard fuel cell operating regimes, where activation and ohmic losses dominate, concentration losses and thus, the tortuosity of the porous layers affect the performance only slightly.

However, experimental based tortuosity values are only valid for the specific experiment at hand. While the results between image and experimental based tortuosity values in the above case are close, this agreement might not be reproducible when the fuel gas composition changes.

Figure 4 also shows that higher temperatures have a positive effect on tortuosity: for each fuel gas composition, the tortuosity is lower at higher a temperature, which can be explained by the higher catalytic activity and faster diffusion rate. Yet, aside of the effect of temperature, the influence of structural parameters such as the layer thickness on the tortuosity of SOFC anodes is of interest. This was investigated by Tsai and Schmidt,[85–87] who, again, applied Jiang and Virkar's approach for this purpose. While they observed the same dependency of tortuosity on H_2 concentration as Brus *et al*.[71], Tsai and Schmidt[87] showed that electrode thickness had no effect on the achieved tortuosity values which is expected for steady state operation.

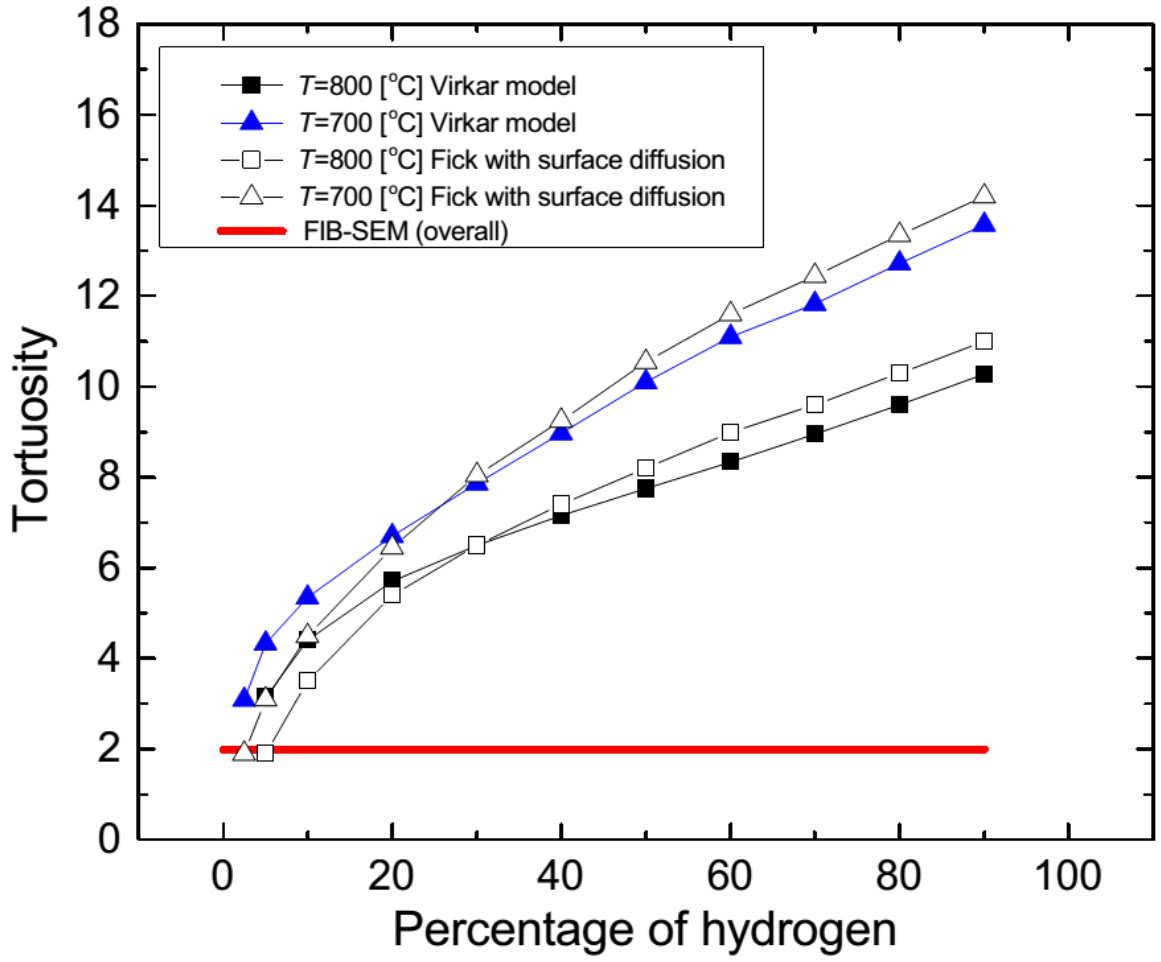

Figure 4: Comparison of experimentally and image based tortuosity values at different temperatures and for varying H_2 concentrations in N_2 [71]

Electrochemical experiments have also been applied to study microstructures of lithium-ion battery materials. Thorat *et al.*[46] used polarization interrupt (or restricted diffusion) experiments[88–90] and impedance spectroscopy to measure the tortuosity in electrode and separator layers. Using the polarization interrupt technique, Thorat *et al.* derived the tortuosity of two distinct active material films consisting of $LiFePO_4$ and $LiCoO_2$, respectively. On the other hand, AC impedance spectroscopy was carried out to determine the effective conductivity of the electrolyte in the separator and ultimately, the MacMullin number or the tortuosity of the separator itself. While the authors used the AC impedance experiments to validate the polarization interrupt experiments, the effect of porosity on the tortuosity of the active material films was in the centre of their research and led to the adjustment of the scaling factor to 1.8 and Bruggeman exponent α to 1.53[46] as discussed in section 3.

With the development of advanced manufacturing techniques, lithium ion battery electrode microstructures can be tailored and optimized to meet user and application specific demands. Bae *et al.*,[91] for example, applied a two pronged approached to improve electrode design: first, using a modified model by Doyle and Newman[92], the tortuosity of different electrode microstructures with periodically spaced flow channels, was calculated. Based on these results, $LiCoO_2$ electrodes mimicking the modelled microstructures were manufactured using a co-extrusion procedure. In their model, electrodes with flow channel spacing equal to or smaller than the electrode thickness offered lowest tortuosity values. To validate these findings, charge and discharge curves of the

manufactured samples with large, medium and small channel spacing were measured. As predicted, the sample with finest and most closely spaced channels yielded highest specific capacity of approximately 8 mAh/cm^2 at C-rates of one and two. The authors attributed this improved capacity to the lower tortuosity of their manufactured electrode, validating their model.

In general, experimental setups can be adjusted to fit the operating conditions of the analysed specimen. However, as the derived results are fitting parameters, the tortuosity values are highly dependent on the applied model. Moreover, while fuel cell experiments can be highly versatile in terms of operating temperature and applied fuel gas, batteries are not subject to such variations. Hence, it appears to be easier to extract an overall valid tortuosity value for a battery layer than a fuel cell layer.

5. Tortuosity Calculation in 3D Volumes

The advent of sophisticated and easily accessible tomography methods has increased the amount of obtainable data of porous samples which fundamentally changed the perception of microstructural characterisation in 3D.[93] Focused ion beam–scanning electron microscope (FIB-SEM) slice and view tomography,[94] and X-ray computed tomography (X-ray CT)[95] are among the most prominent methods of reconstructing a sample in three dimensions. Even though the operation and image acquisition of both method is radically different, comparative studies showed, that acquired data is identical when the resolution is the same.[84,96,97]

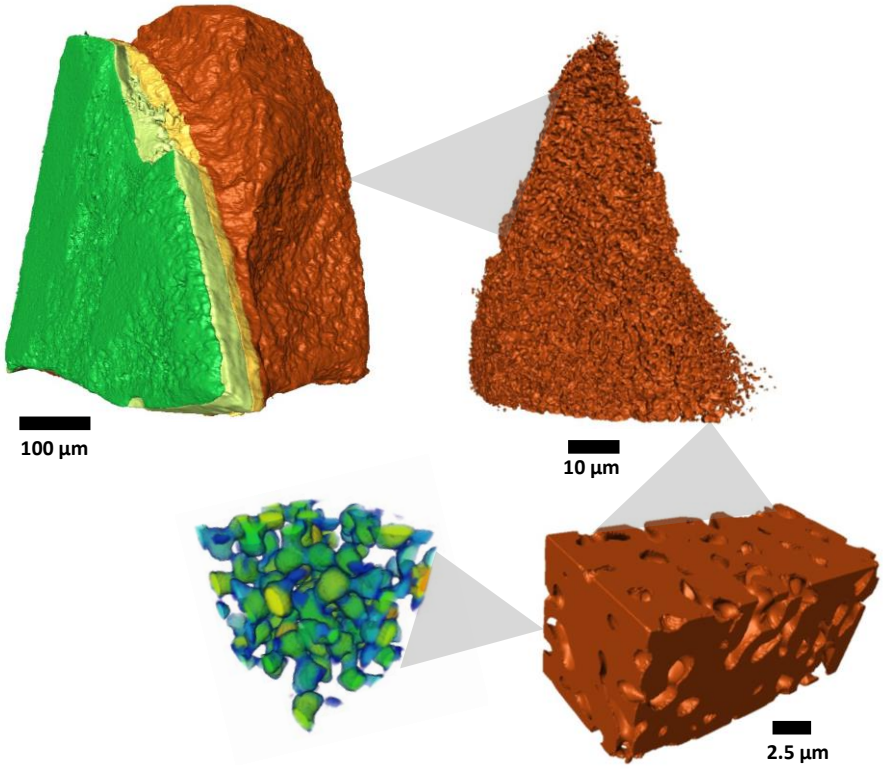

Figure 5: Illustration of increasing resolution of X-ray CT scan of porous support layer of OTM for preparation of diffusion simulation

In recent years, tomographic reconstruction of microstructures in electrochemical devices, illustrated in Figure 5, has become increasingly widespread, offering, the possibility to evaluate vital parameters, such as triple phase boundary length in SOFCs,[98,99] connectivity,[100] phase distribution[101] and tortuosity[80,98] at different length scales.[102] Additionally, the effect of microstructural parameters

on the performance of electrochemical devices has been evaluated by generating synthetic 3D volumes *in-silico*.[33,55,103,104] The purpose for this process is to directly evaluate the effect of specific microstructural variations such as porosity, pore size distribution, shape or packing orientation of particles on mass transport.

There remains some confusion in the literature regarding the different definitions of tortuosity for the purpose of image based modelling: here, we distinguish between two main approaches in extracting tortuosity:

1. Geometric based algorithms, which aim to determine the shortest path length through a porous structure by purely considering geometric aspects.
2. Flux based algorithms, which mimic mass transport and diffusion behaviour, which is not taken into consideration in geometric based algorithms. These methods are further divided into the following two subsections:
    a. Voxel based algorithms that take the extracted dataset and directly execute tortuosity extraction techniques across the voxel domain of the analysed phase.
    b. Mesh based approaches which rely on generating a volume mesh of the analysed phase to prepare the sample for computational fluid dynamics (CFD) programs.

It is evident, that the increase in development of such techniques correlates with the increasing accessibility of tomography equipment and high-performance computers.

5.1. Geometrically Based Algorithms

Geometric algorithms are commonly used to find the shortest pathway through a porous structure and thus, its tortuosity. The pore centroid method,[62,102,105–107] the fast marching method (FMM),[2,108,109] the distance propagation method,[110] as well as or other shortest path search methods[111,112] achieve this by being executed on the voxel domain of the analysed phase. These methods are straightforward in their application, as mesh preparation and refinement is not required. In addition, the results directly follow the initial definition of tortuosity, making them conceptually easier to interprete. Furthermore, apart from the pore centroid method, these algorithms create a distance map, which incorporates the distance of each pixel to the starting plane of the algorithm. Using the resulting distance map allows not only the identification of the shortest pathway, but also the generation of a tortuosity histogram (see Figure 6).

The FMM achieves this by simulating an advancing front starting from one plane of the sample towards the opposite plane in the considered phase. The algorithm measures the time it takes for the front to reach each pixel on its way. By knowing the speed of advance of the front and the time it takes to arrive at a pixel, the distance between each pixel and the starting plane is achieved and tabulated in a distance map. Finally, tortuosity is calculated by dividing the shortest path length between two opposing planes by the Euclidean distance of the two endpoints of that path.

Jørgensen *et al*.[108] exploited the FMM based tortuosity histograms of a strontium-substituted lanthanum cobaltite (LSC) and gadolinia-substituted ceria (CGO) SOFC cathode, shown in Figure 6, to understand microstructural characteristics of each phase. In accordance with each phase's volume fraction, LSC features higher tortuosity values than CGO. The distinct shapes and specifics of each phase's tortuosity achieved by the FMM based histograms are able to provide more insight into the microstructural build-up of a sample compared to a single, mean tortuosity value.

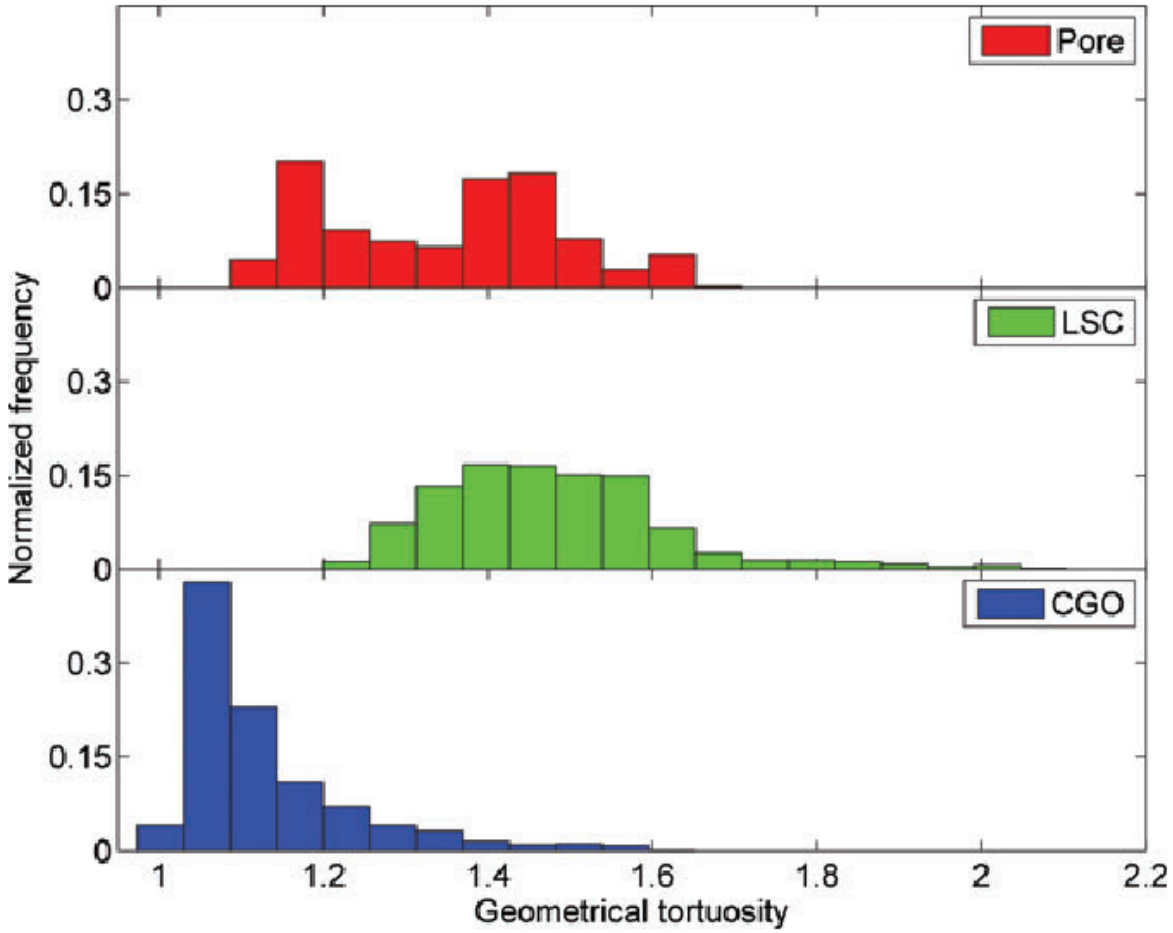

Figure 6: Geometric tortuosity histogram achieved by FMM for all three phases of a SOFC cathode [108]

Yet, tortuosity histograms do not show, where the specific high or low tortuosity values are located within the sample. This, however, was realised by Chen-Wiegart *et al.*,[110] who combined different tomography methods and distance propagation based tortuosity calculation approaches on various samples. Specimens included, among others, a $LiCoO_2$ battery cathode, which was reconstructed using X-ray tomography. Geometric tortuosity values were then achieved by pixel counting and distance measuring techniques. The resulting values were not only represented as tortuosity histograms, similar to the ones presented in Figure 6, but also as 3D distribution across the battery cathode sample, as shown in Figure 7. The local variation in the image slices range from one to 2.5, which can also be ascertained from the tortuosity histogram. However, as tortuosity poses a resistance to mass and charge transport, the local tortuosity distribution is capable of pinpointing areas of low reactivity. It can be used to explain regions of increased charge transfer, areas of low fuel conversion, uneven charging or catalyst utilisation and degradation. Shearing *et al.*[111] extended the approach of spatial distribution of geometric tortuosity to include additional characteristics such as volume specific surface area (VSSA) and porosity. A reconstructed graphite Li-ion battery electrode was segmented into a mosaic of equally sized volumes. For each tile, the aforementioned parameters were calculated and visualized to highlight the relation between them. While in most cases, tiles with high porosity featured low tortuosity, some sub-volumes exhibited low tortuosity paired with low porosity. Even though this combination seems counterintuitive, it emphasizes the complex interrelation between different microstructural parameters which are not always as clear as expected.

For comparative purposes, Chen-Wiegart *et al*. executed a diffusion simulation analogous to the one used in[3] (*cf*. section 5.2.2) across the same sample volumes. It was shown that the results between the distance propagation and diffusion method of the pore phase in the $LiCoO_2$ sample agreed well. However, when applying the same calculation approaches to two SOFC samples, the geometrically derived tortuosity values for the pore and YSZ phases were consistently below the diffusion based tortuosity methods. The difference might stem from the inherent difference between geometric and diffusion based considerations: the geometrically shortest path through a structure is not always the path of least resistance for a flux, owing to the presence of constrictions and pore necks. Further discussion on the differences of these considerations is presented in section 5.2.

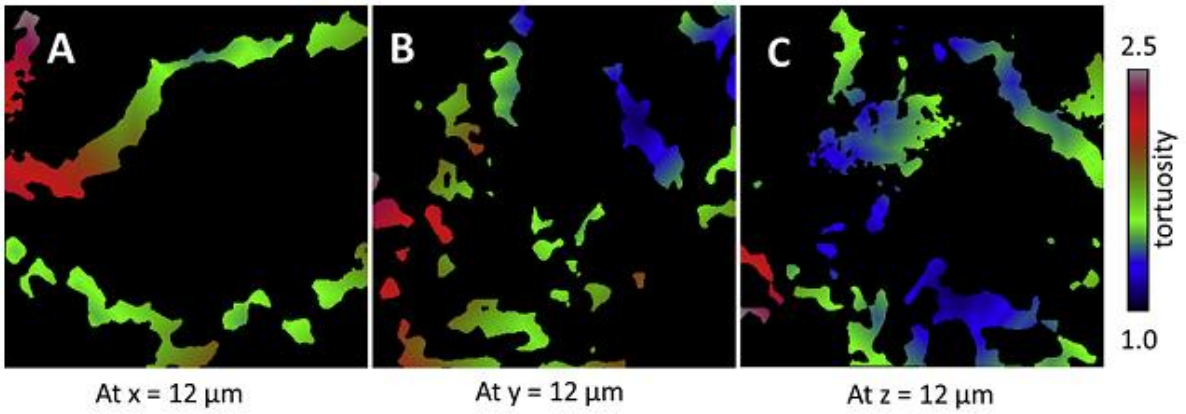

Figure 7: Geometric tortuosity distribution of the pore phase of the $LiCoO_2$ battery cathode of yz (A), xz (B) and xy (C) planes [110]

In contrast to the aforementioned algorithms, the pore centroid method does not provide a histogram of tortuosity values or spatial distribution of tortuosity, but rather arrives at one specific value of tortuosity along each dimension of a sample. The calculation algorithm follows the centre of mass of a phase of a 2D plane along the third axis of the volume. The length of the pathway going through each centroid is then calculated and used to determine the tortuosity as depicted in Figure 8. Despite its shortcomings in comparison with the previous algorithms, the pore centroid is a standard option in image and volume processing programs such as Amira and Avizo (both FEI). As such, it is easily applied for comparative studies and capable of giving a quick tortuosity estimate.

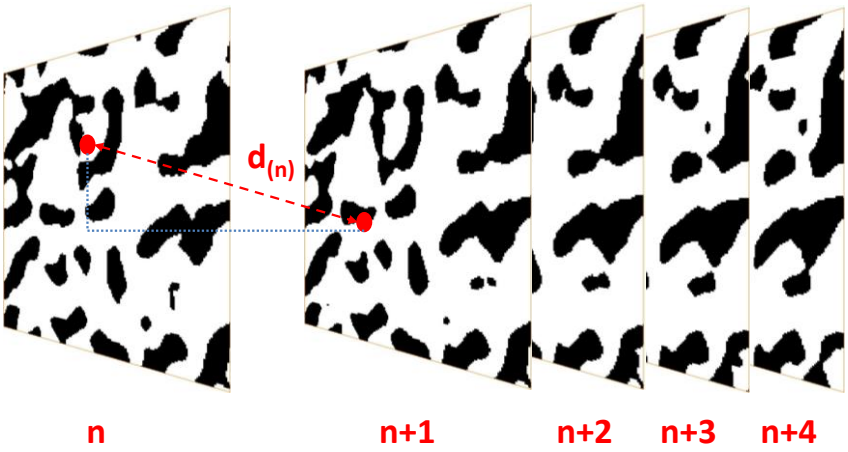

Figure 8: Illustration of the pore centroid method calculation approach which measures the distance $d_{(n)}$ of the centres of mass between two 2D image slices

Cooper *et al.* used the pore centroid method for comparison reasons when studying an SOFC[107] and a battery electrode (*cf.* section 5.2.2).[62] In [107], the tortuosity of the solid and pore phase of an LSCF SOFC cathode was determined by a variety of calculation algorithms, namely heat flux simulation (*cf*. section 5.2.2), Avizo XLab plugin, diffusion simulation (*cf*. section 5.2.1), random walk method (*cf*. section 5.2.1) and pore centroid method. These algorithms were executed across the same sample after imaging at 14 °C and 695 °C using synchrotron X-ray nano CT which have previously been extracted by Shearing *et al*.[113] The pore centroid method produced the lowest tortuosity values for both phases at both temperatures and closely followed the Bruggeman relationship. Yet, the flux based calculation algorithms agreed well with each other as values lay between the heat flux simulation and the random walk method. The average tortuosity for the pore phase amounted to approximately 1.21 in all three dimensions at both temperatures and lay visibly below the values reported by Gostovic *et al*.[105] using the same method. Large variability in homogeneity of a sample significantly affect the results achieved by the pore centroid method causing visible fluctuations. In this respect, Cooper[114] pointed out, that if the analysed characteristic feature becomes small compared to the control volume, the centroid of each 2D plane will tend towards the centre, resulting in a tortuosity of unity which casts doubt on the applicability of this approach.

5.2. Flux Based Algorithms

Even though geometrically based tortuosity calculation algorithms can extract useful data concerning the distribution of geometric tortuosity across a sample, these algorithms do not mimic the flux like behaviour of transport phenomena. For example, small connections consisting only of one voxel would only contribute a negligible amount to the overall flux of transported species while they are fully included in the above calculation methods. As a result, flux based algorithms focus on simulating the transport mechanism at hand to extract the tortuosity of a sample. Here, this method is separated into two parts, namely voxel and mesh based calculation approaches.

5.2.1. Voxel Based Calculation Methods

Voxel based algorithms are directly executed across the voxel domain of the reconstructed volume. This means that for the methods introduced below, no additional re-tessellation or re-meshing steps are necessary after the sample has been segmented. In most cases, a binarised 2D image sequence is sufficient to operate the calculation procedure.

One of the first applications of combining X-ray nano tomography with image based tortuosity calculation was presented by Izzo *et al*.,[80] where X-ray CT was used to gather microstructural parameters of a porous SOFC anode including porosity, tortuosity and pore size distribution. The authors solved the Laplace equation of diffusive mass transport through the pore phase of the electrode as explained in a different publication of the group.[115] Grew *et al*.[116] applied the same methodology but extended its application to the solid phases of a Ni-YSZ SOFC anode. As effective ionic and electronic conductivity are affected by the tortuous nature of fuel cell electrode layers (*cf*. Eq. (2)), tortuosities of solid phases are equally as important as of pore phases. Yet, they were at least a factor of 1.2 higher.

Their work was further refined in[117] by calculating the representative volume element of the pore phase tortuosity by solving the Laplace equation using the same method. Cooper[114] programmed a MATLAB (Mathworks) Laplace solver called *TauFactor*[118] to extract the tortuosity of a two phase segmented 3D tiff stack as shown in Figure 9. The solver then determines the tortuosity in each dimension for both phases. In[114], Cooper compared the results of the *TauFactor* solver to his previous work presented in[107] revealing, that his solver gives similar results as the Avizo package XLab Thermo and the heat flux simulation.

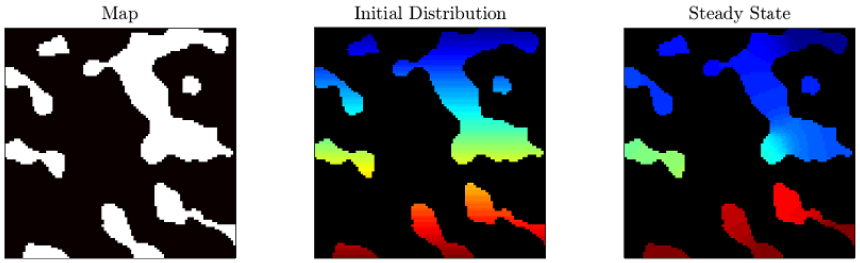

Figure 9: Results of the TauFactor solver by Cooper [114] running across the pore phase of a porous sample showing the binary image map, the initial, linear concentration distribution and the concentration distribution at steady state

Aside from solving the Laplace equation to arrive at the tortuosity of their sample, Izzo *et al*.[80] included the lattice Boltzmann method (LBM)[119] to model multi-component gas transport coupled with an electrochemical model to visualize the H_2 distribution in the anode. Due to the capability to model gaseous, ionic and electronic transport, the LBM became widely applied in fuel cell research also with the focus of extracting tortuosity in different phases of a functional layer.[99,120–125] For this, the LBM uses the particle distribution function (PDF) $f^i_{\alpha_{PDF}}$, which is a function describing the probability of encountering a particle of a species *i* at a certain location x_{PDF} with a certain speed $e^i_{\alpha_{PDF}}$ at a certain point of time *t* moving in a certain direction α_{PDF}.

The LBM consists of two steps, namely streaming and collision, which are carried out on each point of a lattice: during streaming, the particles migrate to adjacent lattice points while during collision, the interactions between particles at each lattice point governed by the collision term $\Omega^i_{\alpha_{PDF}}$ are computed. Both steps are collectively expressed by the lattice Boltzmann equation:[115,126]

$$f^i_{\alpha_{PDF}}\left(x_{PDF} + e^i_{\alpha_{PDF}}, t+1\right) - f^i_{\alpha_{PDF}}(x_{PDF}, t) = \Omega^i_{\alpha_{PDF}} \qquad \text{Eq. (16)}$$

Using this approach, Iwai *et al*.[99] arrived at tortuosity values for each phase in the porous Ni-YSZ anode by calculating the effective diffusion coefficient and effective ionic as well as electronic conductivities of the respective phases. The anode sample was reconstructed based on FIB-SEM tomography, where the Ni and YSZ phases were identified via EDX mapping, to correlate the correct phase to the respective electron image. Table 2 compares the achieved tortuosity values for all three phases along each dimension using the LBM as well as the random walk method, which is introduced thereafter. It is evident, that the tortuosity values of the solid phases are higher compared to the pore phase, which is identical to findings presented by Chen-Wiegart *et al.*[110] using a distance mapping approach. Nevertheless, values for the pore phase tortuosity are lower but comparable to values found by Izzo *et al*.[80] However, due to the observed directional anisotropy of the solid phase tortuosities, Iwai *et al*. concluded, that the sample volume was not sufficiently large to present effective ionic and electronic conductivity values. Vivet *et al*.[127] achieved similarly high Ni-phase tortuosity values using a finite difference method. However, due to the higher YSZ fraction in their sample, achieved YSZ tortuosities lay below the values reported by Iwai *et al*.[99]

The aforementioned random walk method[28,99,128–131] mimics a diffusion process by distributing a number of non-sorbing particles, so-called “walkers”, across the segmented voxel phase. The algorithm then starts a time step sequence, where at each step, every walker choses one neighbouring voxel as its next location. If that neighbouring voxel is of the same phase (e.g. pore phase), the walker migrates to that new location. However, if the chosen neighbouring voxel is of a different phase (e.g. solid phase), the walker remains at its current location and choses a different neighbouring voxel at the following time step. By repeating this sequence, the mean square

displacement $\langle r^2(t)\rangle$ of the walkers in the analysed phase is calculated which, in turn, is used to achieve an effective diffusion coefficient D^{eff}, where V_{phase} is the volume fraction of the analysed phase:

$$D^{eff} = \frac{V_{phase}}{6} \frac{d\langle r^2(t)\rangle}{dt} \quad \text{Eq. (17)}$$

Tortuosity is then calculated by comparing the effective diffusion coefficient to the bulk diffusion coefficient through an empty volume of equal dimensions. The random walk approach was first formulated in the 1990s[4,132,133] and found its way into electrochemistry via Kishimoto *et al.*,[128] after having been used to extract the tortuosity of porous rocks.[134] However, the obtained tortuosity is affected by the number of walkers and by the number of time steps chosen for the calculation. This is why, in[99], 100,000 walkers and 10,000,000 time steps are chosen to ensure high accuracy of the results (*cf*. Table 2).

Table 2: Tortuosity values for pore, Ni and YSZ phase of an SOFC anode calculated using the random walk method and LBM [99]

		Random walk method	Lattice Boltzmann method
Pore phase	*x*	1.43	1.42
	y	1.41	1.44
	z	1.33	1.35
Nickel phase	*x*	4.70	4.66
	y	5.43	5.43
	z	2.63	2.63
YSZ phase	*x*	5.28	5.26
	y	3.87	3.85
	z	3.14	3.14

A similar, comparative study using the random walk method was carried out by Tariq *et al*.[131] The tortuosity values of a Li-ion battery anode calculated by the random walk method was compared to results based on a sub-grid scale finite volume method explained by Kishimoto *et al*.[135] As shown in Table 3, results for both methods agree excellently, revealing a higher tortuosity along the *z*-axis of the pore phase. The authors noted, that a representative volume element (RVE) analysis would reveal, if this anisotropy was persistent or if the high value was caused by a local heterogeneity. Yet, it was noted, that the computation time needed for the random walk method is only a fraction compared to the finite volume method.

Table 3: Tortuosity values for graphite and pore phase using the random walk method and finite volume method [131]

		Random walk method	Finite volume method
Graphite phase	*x*	1.57	1.56
	y	1.92	1.89
	z	2.59	2.57
Pore phase	*x*	1.42	1.42
	y	1.19	1.18
	z	2.39	2.37

5.2.2. Mesh Based Calculation Methods

By applying the same tomography methods mentioned in the previous section, extracted datasets can be represented as volume meshes for additional analysis algorithms enabled, for example, by CFD or finite element software packages. These programs allow the simulation of heat, mass and/or charge transport through the generated mesh of the investigated structure to subsequently evaluate the tortuosity. In the data preparation process, parameters chosen for sample smoothing, surface repair and mesh generation affect mesh quality and thus the simulation results. Hence, care must be taken when choosing these parameters[84] and sensitivity analyses should be carried out to verify the consistency of the chosen values.

Pioneering work in this field was realized by Wilson *et al*.,[98] who reconstructed an SOFC anode using FIB-SEM tomography. The tortuosity of the pore phase was then extracted to assess the mass transport limitations at high current densities. For this, the sample volume was converted into a finite element mesh to solve the Laplace equation in FEMLAB (now COMSOL Multiphysics).

Extensive simulation work in the field of electrochemical devices using a similar approach as presented above has been carried out by Ivers-Tiffée and co-workers: initially based on COMSOL Multiphysics, the group developed the 3D finite element tool *ParCell3D* to model the behaviour of fuel cells[136–139] and batteries.[140] Joos *et al*.[141] used this tool to investigate the representative volume element of tortuosity of an SOFC cathode for both phases, namely the pore and the mixed ionic-electronic conducting LSCF phase. In total, the RVE of porosity, volume specific surface area and tortuosity were calculated for three separate volumes, of which the latter one is presented in Figure 10. The results for both phases in sample volumes 1 and 3 agree excellently with each other, achieving a flat development for electrode thicknesses of $l_{cat} > 10$ µm. However, the tortuosity of the LSCF phase in sample two takes an electrode thickness almost twice as long as for the other sample volumes to produce a flat curve. To follow the nomenclature of this review, it has to be pointed out, that τ in Figure 10 ought to be replaced by τ^2.

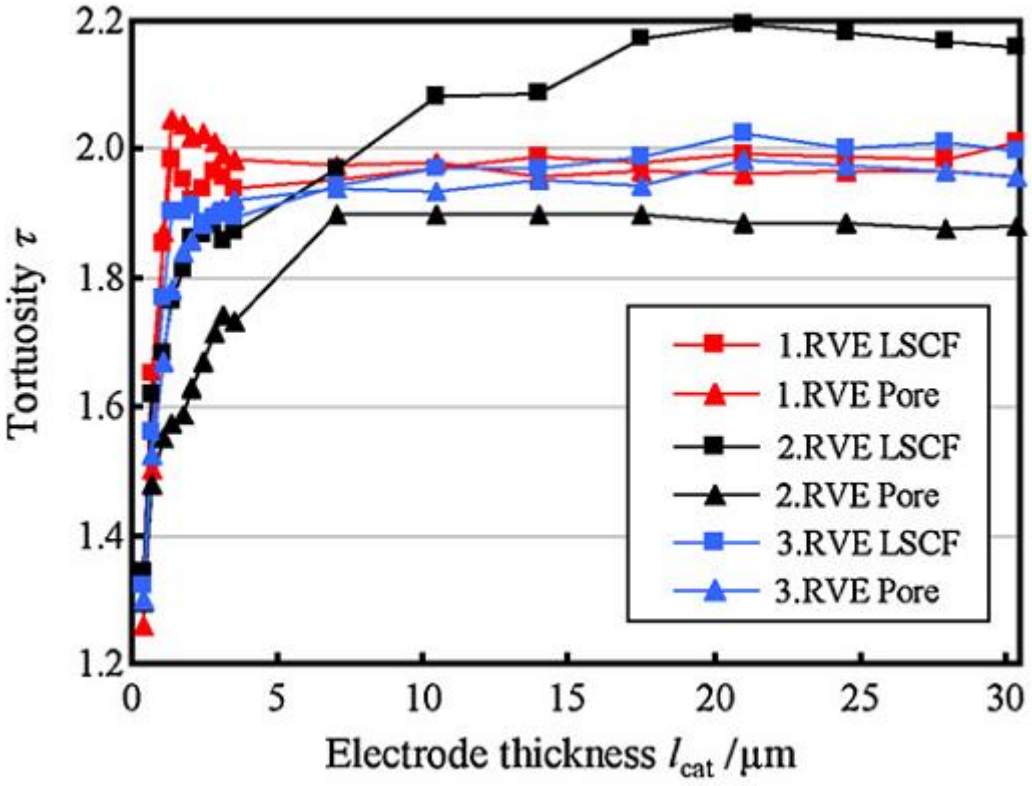

Figure 10: Representative volume element analysis of the tortuosity factor for the pore and LSCF phase of an SOFC cathode as function of electrode thickness [141]

Besides COMSOL Multiphysics,[142,143] researchers have calculated tortuosity by using programs such as Cast3M[144] or custom made models, which focus on a specific electrochemical device, such as *Batts3d*.[33,55,145]

In addition to simulating mass and charge transport, the tortuosity is also computable by exploiting the mathematical similarity between Fourier's law of heat conduction and Fick's law of diffusion shown in Eq. (18) and Eq. (19), where J_{eff} is the effective diffusion flux, c is the molar concentration, $\dot{q}_{eff}$ is the effective heat flux, λ^{bulk} is the bulk thermal conductivity.[84,102,146,147] By rearranging the temperature gradient, the heat flux and thus, the tortuosity can be calculated along each axis of a sample. Cooper *et al.*[62] scanned a commercially available $LiFePO_4$ battery cathode using X-ray synchrotron nano CT and investigated the tortuosity of the pore phase using heat flux simulation. A cube of 8.8 µm side length was cropped and meshed using an adaptive polyhedral volume mesh. The heat flux across the porous phase of the sample was simulated in StarCCM+ (CD-adapco) resulting in a temperature distribution across the analysed volume (see Figure 11), where the temperature of each mesh element can be understood as a concentration value of a migrating species.

$$J_{eff} = -D^{bulk}\,\frac{\varepsilon}{\tau^2}\,\frac{(c_1 - c_2)}{d} \qquad \text{Eq. (18)}$$

$$\dot{q}_{eff} = -\lambda^{bulk}\,\frac{\varepsilon}{\tau^2}\,\frac{(T_1 - T_2)}{d} \qquad \text{Eq. (19)}$$

For further analysis, the sample was divided into eight non-overlapping sub-samples to compare the pore centroid and heat flux based tortuosity factors. To extract a single tortuosity value for each sub-volume, the concept of the characteristic tortuosity τ_C was introduced:[62,84]

$$\tau_c = 3 * \left[\left(\tau_x{}^{-1}\right) + \left(\tau_y{}^{-1}\right) + \left(\tau_z{}^{-1}\right)\right]^{-1} \quad \text{Eq. (20)}$$

The geometric based characteristic tortuosity factors (κ_{geo}) were then plotted as a function of the flux based characteristic tortuosity factors (κ_{flux}). The resulting graph revealed a high degree of correlation following the equation Eq. (21). This equation reveals, that the simulation based tortuosity factor (and as such, tortuosity) is always higher than the geometric based value of the same sample in cases, where either value is > 1. As mentioned previously, geometric tortuosity algorithms do not take the effect of pore constrictions into account, which would affect a transport flux. This means that any connection consisting of only one voxel in diameter is fully considered in the calculation process while from a flux point of view, such a pore would not allow a significant amount of mass/charge to pass through. As a result, geometric based tortuosity values tend to be visibly lower compared to simulation based values.[62,84]

$$\kappa_{geo} = 0.5 \; ln\left(\kappa_{flux}\right) + 1 \quad \text{Eq. (21)}$$

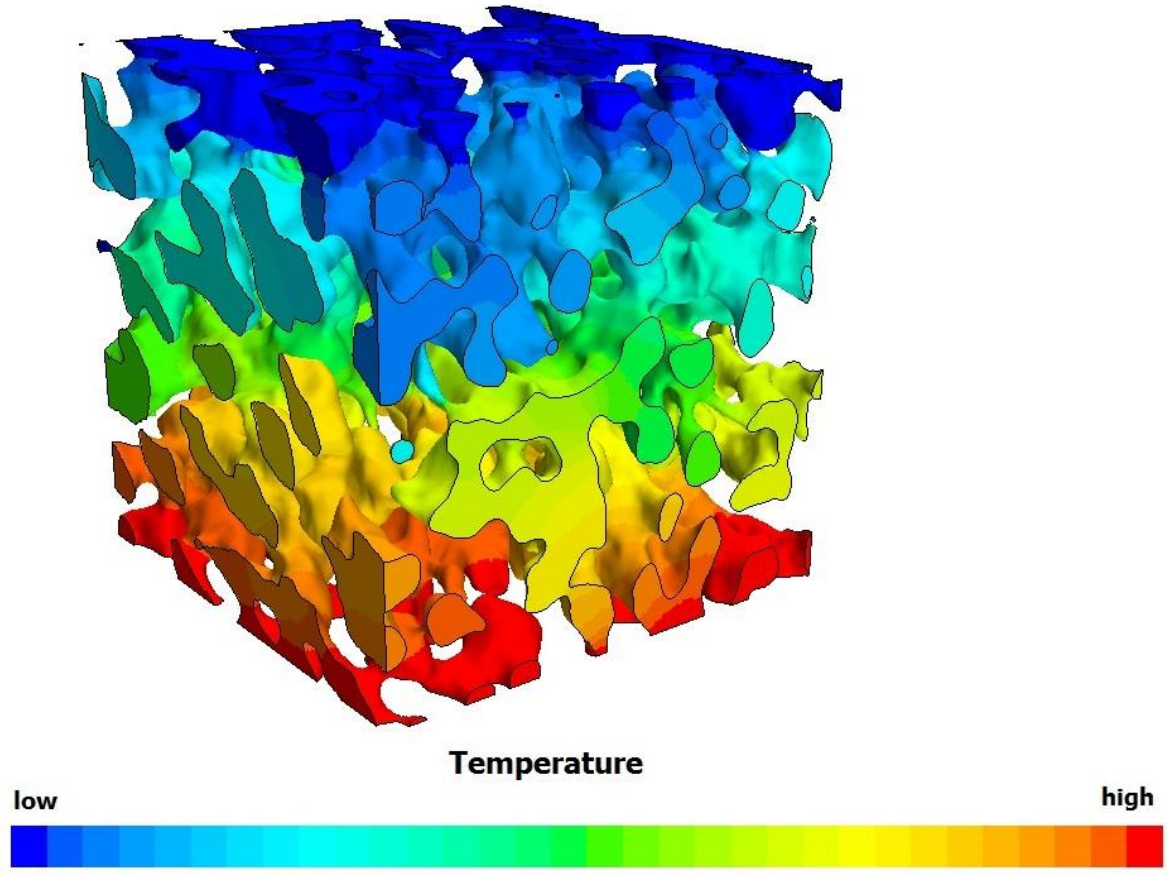

Figure 11: Temperature distribution across the porous phase of an YSZ porous support membrane of an oxygen transport membrane

It is common practice to subdivide a given sample volume into an array of smaller sub-samples and extract the tortuosity for each individually.[50,141,148] Although non-trivial, this approach allows to extract similar conclusions as tortuosity histograms and tortuosity distribution maps (cf. section 5.1) using flux based methods. This approach reveals the homogeneity or heterogeneity of a sample, similar to tortuosity histograms, and pinpoints the locations of high or low tortuosity. Kehrwald *et*

al.[50] were among the first ones to apply this methodology on a battery electrode by solving Fick's law using the program Star-CD (CD-adapco) on a total of twelve sub-volumes. Local tortuosities showed differences of a factor of three, which might lead to inefficiencies during charging and discharging of the battery: Li^+ ions will avoid areas with higher tortuosity, but seek areas with low tortuosity highlighting the need of homogeneous microstructures in this field to avoid uneven degradation.[148] In addition, microstructural inhomogeneities might be the cause of failure mechanisms and material fractures.[50]

5.3. Summary

Table 4 lists pore phase tortuosity factors and tortuosity values for different image based calculation methods along all three axes of porous samples. Calculation approaches which only take geometric aspects into consideration show slightly lower values compared to flux based algorithms. It is thus imperative to distinguish between these two approaches as otherwise, misinterpretation may ensue. Furthermore, differences in tortuosity values are observed even when analysing the same type of samples. This can be explained by the chosen imaging resolution; higher resolution uncovers smaller pore structures and improves pore connectivity. This way, lower tortuosity values are obtained.[102] This finding is comparable to the analogy by Mandelbrot[149] who stated that the length of a coastline is depending on the resolution of the map. Moreover, the size of the sample volume has to be sufficiently large so that extracted values are representative of the sample bulk.[150] Hence, the higher the resolution, and the larger the extracted volume, the more likely the extracted values are accurate, and representative, and not affected by microscopic heterogeneities.

However, when comparing the work by Wilson *et al*.[98] and Iwai *et al*.[99], who analysed the same type of sample using the same imaging technique achieving similar pixel sizes, no difference in tortuosities is observed even though Iwai *et al*. reconstructed a nine times larger sample volume. Similar findings are revealed when comparing Laurencin *et al.*[144] and Tjaden *et al*.[84] Yet, this does not contradict the previous statement as homogeneous samples will yield representative values even for small sample volumes.

In addition, the above comparison revealed that different flux based tortuosity calculation algorithms yield comparable results, which was also affirmed when executing different algorithms on the exact same sample.[99,131] This suggests that the choice of a flux based computation algorithm has a smaller effect on the results than sample preparation technique, imaging parameters and the structure of the sample itself, which includes pore size distribution and volume fractions of the constituent phases. The interplay between these additional parameters and the tortuosity is visible when inspecting the work by Wilson *et al*.[98] and Izzo *et al*.[80]: while Izzo *et al*. presented higher tortuosity values, the porosity of their sample is a factor of 1.5 higher. Hence, the tortuosity itself does not give a full picture of the microstructure and the performance of the analysed sample, but has to be evaluated with respect to other microstructural characteristics.[111,151] Also, care must be taken when applying purely continuum based models which do not account for Knudsen diffusion effects, such as the heat flux simulation. Such simplifications might cause visible differences between experimental and simulation based results.[84]

Table 4: Comparison of differently calculated tortuosity values along each dimension for pore phases of porous membranes

Calculation Method	Sample	Tomography Technique	Pixel Size	Sample Volume	Porosity	Dimension	τ^2	τ	Reference
			[µm]	[µm^3]	[-]		[-]	[-]	
Laplace equation	Ni-YSZ based SOFC anode	FIB-SEM	0.0417	105.2	0.195	*x*	2.10	1.45	Wilson *et al.*[98]
						y	2.20	1.48	
						z	1.90	1.38	
Laplace equation	Ni-YSZ based SOFC anode	X-ray	0.0427	250.0	0.300	*x*	2.94	1.71	Izzo *et al.*[80]
						y	3.28	1.81	
						z	3.15	1.77	
Laplace equation	Ni-YSZ based SOFC anode	X-ray	0.008	13.8	0.180	*x*	1.77	1.33	Grew *et al.*[116]
						y	1.51	1.23	
						z	Not presented		
Finite volume method	Mesocarbon microbead based battery electrode	X-ray	0.016	1,100.0	0.451	*x*	2.01	1.42	Tariq *et al.*[131]
						y	1.39	1.18	
						z	5.61	2.37	
Lattice Boltzmann method	Ni-YSZ based SOFC anode	FIB-SEM	0.062	972.4	0.496	*x*	2.03	1.42	Iwai *et al.*[99]
						y	2.06	1.44	
						z	1.83	1.35	
Random walk method	Ni-YSZ based SOFC anode	FIB-SEM	0.062	972.4	0.496	*x*	2.05	1.43	Iwai *et al.*[99]
						y	1.99	1.41	
						z	1.78	1.33	
Random walk method	Mesocarbon microbead based battery electrode	X-ray	0.016	1,100.0	0.451	*x*	2.03	1.42	Tariq *et al.*[131]
						y	1.41	1.19	
						z	5.72	2.39	
Heat flux simulation	$LiFePO_4$ based battery electrode	X-ray	0.020	3,000	0.410	*x*	2.70	1.64	Cooper *et al.*[62]
						y	2.19	1.48	
						z	3.32	1.82	
Heat flux simulation		FIB-SEM	0.030	421.9	0.350	*x*	2.82	1.68	Tjaden *et al.*[84]
						y	2.72	1.65	

	YSZ based porous support layer					*z*	3.10	1.76	
Heat flux simulation	YSZ based porous support layer	X-ray	0.0325	314.4	0.410	*x*	3.13	1.77	Tjaden *et al*.[84]
						y	2.25	1.50	
						z	2.96	1.72	
Heat flux simulation	$LiMn_2O_4$ based battery electrode	X-ray	0.597	10,434,731	0.363	*x*	8.29	2.88	Shearing *et al*.[102]
						y	2.31	1.52	
						z	4.97	2.23	
Heat flux simulation	$LiMn_2O_4$ based battery electrode	X-ray	0.065	75,164	0.380	*x*	6.50	2.55	Shearing *et al*.[102]
						y	2.22	1.49	
						z	3.96	1.99	
Laplace equation	LSCF based SOFC cathode	FIB-SEM	0.035	144.7	0.483	*x*	1.82	1.35	Joos *et al.*[141]
						y	1.83	1.35	
						z	1.88	1.37	
Laplace equation	YSZ based porous support layer	X-ray	0.060	46,656	0.470	*x*	2.30	1.52	Laurencin *et al.*[144]
						y	2.80	1.67	
						z	2.60	1.61	
Fast marching method	YSZ based porous support layer	FIB-SEM	0.030	421.9	0.350	*x*	1.42	1.19	Tjaden *et al*.[84]
						y	1.25	1.12	
						z	1.23	1.11	
Fast marching method	YSZ based porous support layer	X-ray	0.0325	314.4	0.410	*x*	1.44	1.20	Tjaden *et al*.[84]
						y	1.25	1.12	
						z	1.19	1.09	
Pore Centroid Method	$LiFePO_4$ based battery electrode	X-ray	0.020	3,000	0.410	*x*	1.46	1.21	Cooper *et al*.[62]
						y	1.41	1.19	
						z	1.58	1.26	

6. Concluding Remarks

The large number of tortuosity calculation methods is testimony of the significance of tortuosity in the field of electrochemistry. Here we have reviewed different tortuosity calculation approaches which span from porosity-tortuosity correlations and image based techniques to experimental methods. Among these, a certain trend is revealed: porosity-tortuosity relationships, such as the Bruggeman equation, are more common in battery and PEM research, while flux based algorithms are popular in SOFC research. Yet, each approach features distinct advantages and disadvantages. While easily applied, the Bruggeman relationship is only valid for spherical structures and unfit to predict accurate values for complex porous networks. When applying image based tortuosity calculation algorithms, one must be aware of the difference and significance of geometric and flux based tortuosity. Results of either calculation procedure differ visibly, where geometric values lie below flux based algorithms. Moreover, tortuosity values determined using experimental techniques are only valid for the specific experiment at hand, as changes in temperature, setup and gas composition affect the results. Also, tortuosity is usually used as a fitting parameter in these cases, making it highly dependent on the applied calculation model. Furthermore, when comparing flux based algorithms across similar sample types, it is shown, that tortuosity is a complex function of microstructural parameters and has to be interpreted while taking pore size distribution and volume fraction of constituents into consideration. However, purely continuum based models which do not consider Knudsen effects have to be applied with caution as they might be the reason for discrepancies between simulation and experimental values. Also, a unifying tortuosity calculation approach would be highly useful to make values, structures and manufacturing techniques across the field of electrochemistry comparable. For this, imaged based methods are most applicable as they can be applied to all types of microstructures and devices. Even though experimental approaches provide more practical results as their setup can be tailored to the actual operating conditions, image based methods are independent of the functionality or non-functionality of the specimen. However, sample volume and resolution have to be sufficiently high to result in representative values.

7. Acknowledgements

8. References

1. P.R. Shearing, D.J.L. Brett, N.P. Brandon: 'Towards intelligent engineering of SOFC electrodes: a review of advanced microstructural characterisation techniques', *Int. Mater. Rev.*', 2010, **55**, (6), 347–363.
2. O.O. Taiwo, D.P. Finegan, D.S. Eastwood, J.L. Fife, L.D. Brown, J.A. Darr, P.D. Lee, D.J.L. Brett, P.R. Shearing: 'Comparison of three-dimensional analysis and stereological techniques for quantifying lithium-ion battery electrode microstructures', *J. Microsc.*', 2016, n/a.
3. J.R. Wilson, S.A. Barnett: 'Solid Oxide Fuel Cell Ni–YSZ Anodes: Effect of Composition on Microstructure and Performance', *Electrochem. Solid-State Lett.*', 2008, **11**, (10), B181.
4. B. Clennell: 'Tortuosity: a guide through the maze', *Geological Society, London, Special Publications*', 1997, **122**, (1), 299–344.
5. B. Ghanbarian, A.G. Hunt, R.P. Ewing, M. Sahimi: 'Tortuosity in Porous Media: A Critical Review', *Soil Sci. Soc. Am. J.*', 2013, **77**, (5), 1461.
6. M. Mench: 'Fuel cell engines, John Wiley & Sons, Hoboken, N.J, 2008.

7. C. Daniel, J.O. Besenhard (Eds.): 'Handbook of Battery Materials, 2nd ed., Wiley-VCH Verlag GmbH & Co. KGaA, Weinheim, 2011.
8. J. Newman, W. Tiedemann: 'Porous-electrode theory with battery applications', *AIChE J.*', 1975, **21**, (1), 25–41.
9. S. Adler, J. Lane, B. Steele: 'Electrode Kinetics of Porous Mixed-Conducting Oxygen Electrodes', *J. Electrochem. Soc.*', 1996, **143**, (11), 3554–3564.
10. N. Epstein: 'On tortuosity and the tortuosity factor in flow and diffusion through porous media', *Chem. Eng. Sci.*', 1989, **44**, (3), 777–779.
11. J. van Brakel, P. Heertjes: 'Analysis of diffusion in macroporous media in terms of a porosity, a tortuosity and a constrictivity factor', *Int. J. Heat Mass Transfer*', 1974, **17**, (9), 1093–1103.
12. L. Holzer, D. Wiedenmann, B. Münch, L. Keller, M. Prestat, P. Gasser, I. Robertson, B. Grobéty: 'The influence of constrictivity on the effective transport properties of porous layers in electrolysis and fuel cells', *J. Mater. Sci.*', 2013, **48**, (7), 2934-2952.
13. D. Wiedenmann, L. Keller, L. Holzer, J. Stojadinović, B. Münch, L. Suarez, B. Fumey, H. Hagendorfer, R. Brönnimann, P. Modregger, M. Gorbar, U.F. Vogt, A. Züttel, F. La Mantia, R. Wepf, B. Grobéty: 'Three-dimensional pore structure and ion conductivity of porous ceramic diaphragms', *AIChE J.*', 2013, **59**, (5), 1446–1457.
14. W. Kast, C.-R. Hohenthanner: 'Mass transfer within the gas-phase of porous media', *Int. J. Heat Mass Transfer*', 2000, **43**, (5), 807–823.
15. Y. Jiang, A. Virkar: 'Fuel Composition and Diluent Effect on Gas Transport and Performance of Anode-Supported SOFCs', *J. Electrochem. Soc.*', 2003, **150**, (7), A942.
16. J. Hoogschagen: 'Diffusion in Porous Catalysts and Adsorbents', *Ind. Eng. Chem.*', 1955, **47**, (5), 906–912.
17. N. Zamel, N. Astrath, X. Li, J. Shen, J. Zhou, F. Astrath, H. Wang, Z.-S. Liu: 'Experimental measurements of effective diffusion coefficient of oxygen–nitrogen mixture in PEM fuel cell diffusion media', *Chem. Eng. Sci.*', 2010, **65**, (2), 931–937.
18. R. Flückiger, S.A. Freunberger, D. Kramer, A. Wokaun, G.G. Scherer, F.N. Büchi: 'Anisotropic, effective diffusivity of porous gas diffusion layer materials for PEFC', *Electrochim. Acta*', 2008, **54**, (2), 551–559.
19. D. Kramer, S.A. Freunberger, R. Flückiger, I.A. Schneider, A. Wokaun, F.N. Büchi, G.G. Scherer: 'Electrochemical diffusimetry of fuel cell gas diffusion layers', *J. Electroanal. Chem.*', 2008, **612**, (1), 63–77.
20. R.B. MacMullin, G.A. Muccini: 'Characteristics of porous beds and structures', *AIChE J.*', 1956, **2**, (3), 393–403.
21. D. Djian, F. Alloin, S. Martinet, H. Lignier, J.Y. Sanchez: 'Lithium-ion batteries with high charge rate capacity: Influence of the porous separator', *J. Power Sources*', 2007, **172**, (1), 416–421.
22. M.J. Martínez, S. Shimpalee, J.W. Van Zee: 'Measurement of MacMullin Numbers for PEMFC Gas-Diffusion Media', *J. Electrochem. Soc.*', 2009, **156**, (1), B80.
23. J. Landesfeind, J. Hattendorff, A. Ehrl, W.A. Wall, H.A. Gasteiger: 'Tortuosity Determination of Battery Electrodes and Separators by Impedance Spectroscopy', *J. Electrochem. Soc.*', 2016, **163**, (7), A1373.
24. L. Shen, Z. Chen: 'Critical review of the impact of tortuosity on diffusion', *Chem. Eng. Sci.*', 2007, **62**, (14), 3748–3755.
25. D.A.G. Bruggeman: 'Berechnung verschiedener physikalischer Konstanten von heterogenen Substanzen. I. Dielektrizitätskonstanten und Leitfähigkeiten der Mischkörper aus isotropen Substanzen', *Ann. Phys.*', 1935, **416**, (7), 636–664.
26. B. Tjaden, S.J. Cooper, D.J.L. Brett, D. Kramer, P.R. Shearing: 'On the origin and application of the Bruggeman correlation for analysing transport phenomena in electrochemical systems', *Curr. Opin. Chem. Eng.*', 2016, **12**, 44–51.
27. J. Maxwell: 'A treatise on electricity and magnetism, Clarendon press, Oxford, 1873.

28. C.C. Chueh, A. Bertei, J.G. Pharoah, C. Nicolella: 'Effective conductivity in random porous media with convex and non-convex porosity', *Int. J. Heat Mass Transfer*', 2014, **71**, (0), 183–188.
29. R. Rue, C. Tobias: 'On the Conductivity of Dispersions', *J. Electrochem. Soc.*', 1959, **106**, (9), 827–833.
30. T.F. Fuller, M. Doyle, J. Newman: 'Simulation and Optimization of the Dual Lithium Ion Insertion Cell', *J. Electrochem. Soc.*', 1994, **141**, (1), 1–10.
31. P. Arora, M. Doyle, A.S. Gozdz, R.E. White, J. Newman: 'Comparison between computer simulations and experimental data for high-rate discharges of plastic lithium-ion batteries', *J. Power Sources*', 2000, **88**, (2), 219–231.
32. M. Doyle, J. Newman: 'The use of mathematical modeling in the design of lithium/polymer battery systems', *Electrochim. Acta*', 1995, **40**, (13–14), 2191–2196.
33. B. Vijayaraghavan, D.R. Ely, Y.-M. Chiang, R. García-García, E.R. García: 'An Analytical Method to Determine Tortuosity in Rechargeable Battery Electrodes', *J. Electrochem. Soc.*', 2012, **159**, (5), A548.
34. D. Miranda, C.M. Costa, A.M. Almeida, S. Lanceros-Méndez: 'Modeling separator membranes physical characteristics for optimized lithium ion battery performance', *Solid State Ionics*', 2015, **278**, 78–84.
35. D.M. Bernardi, M.W. Verbrugge: 'Mathematical model of a gas diffusion electrode bonded to a polymer electrolyte', *AIChE J.*', 1991, **37**, (8), 1151–1163.
36. G. Lin, W. He, T. van Nguyen: 'Modeling Liquid Water Effects in the Gas Diffusion and Catalyst Layers of the Cathode of a PEM Fuel Cell', *J. Electrochem. Soc.*', 2004, **151**, (12), A1999.
37. J.G. Pharoah, K. Karan, W. Sun: 'On effective transport coefficients in PEM fuel cell electrodes: Anisotropy of the porous transport layers', *J. Power Sources*', 2006, **161**, (1), 214–224.
38. P.K. Das, X. Li, Z.-S. Liu: 'Effective transport coefficients in PEM fuel cell catalyst and gas diffusion layers: Beyond Bruggeman approximation', *Appl. Energy*', 2010, **87**, (9), 2785–2796.
39. J. Marquis, M.-O. Coppens: 'Achieving ultra-high platinum utilization via optimization of PEM fuel cell cathode catalyst layer microstructure', *Chem. Eng. Sci.*', 2013, **102**, 151–162.
40. L.M. Pant, S.K. Mitra, M. Secanell: 'A generalized mathematical model to study gas transport in PEMFC porous media', *Int. J. Heat Mass Transfer*', 2013, **58**, (1–2), 70–79.
41. S. Chaudhary, V.K. Sachan, P.K. Bhattacharya: 'Two dimensional modelling of water uptake in proton exchange membrane fuel cell', *Int. J. Hydrogen Energy*', 2014, **39**, (31), 17802–17818.
42. L. Xing, X. Liu, T. Alaje, R. Kumar, M. Mamlouk, K. Scott: 'A two-phase flow and non-isothermal agglomerate model for a proton exchange membrane (PEM) fuel cell', *Energy*', 2014, **73**, 618–634.
43. L. Xing, M. Mamlouk, R. Kumar, K. Scott: 'Numerical investigation of the optimal Nafion® ionomer content in cathode catalyst layer: An agglomerate two-phase flow modelling', *Int. J. Hydrogen Energy*', 2014, **39**, (17), 9087–9104.
44. W. Wu, F. Jiang: 'Microstructure reconstruction and characterization of PEMFC electrodes', *Int. J. Hydrogen Energy*', 2014, **39**, (28), 15894–15906.
45. T. DuBeshter, P.K. Sinha, A. Sakars, G.W. Fly, J. Jorne: 'Measurement of Tortuosity and Porosity of Porous Battery Electrodes', *J. Electrochem. Soc.*', 2014, **161**, (4), A599.
46. I. Thorat, D.E. Stephenson, N. Zacharias, K. Zaghib, J. Harb, D. Wheeler: 'Quantifying tortuosity in porous Li-ion battery materials', *J. Power Sources*', 2009, **188**, (2), 592–600.
47. M. Doyle, J. Newman, A.S. Gozdz, C.N. Schmutz, J.-M. Tarascon: 'Comparison of Modeling Predictions with Experimental Data from Plastic Lithium Ion Cells', *J. Electrochem. Soc.*', 1996, **143**, (6), 1890–1903.
48. K.K. Patel, J.M. Paulsen, J. Desilvestro: 'Numerical simulation of porous networks in relation to battery electrodes and separators', *J. Power Sources*', 2003, **122**, (2), 144–152.

49. P. Arora, Z. Zhang: 'Battery Separators', *Chem. Rev.*', 2004, **104**, (10), 4419–4462.
50. D. Kehrwald, P.R. Shearing, N.P. Brandon, P.K. Sinha, S.J. Harris: 'Local Tortuosity Inhomogeneities in a Lithium Battery Composite Electrode', *J. Electrochem. Soc.*', 2011, **158**, (12), A1393-A1399.
51. J. Cannarella, C.B. Arnold: 'Ion transport restriction in mechanically strained separator membranes', *J. Power Sources*', 2013, **226**, 149–155.
52. N.A. Zacharias, D.R. Nevers, C. Skelton, K. Knackstedt, D.E. Stephenson, D.R. Wheeler: 'Direct Measurements of Effective Ionic Transport in Porous Li-Ion Electrodes', *J. Electrochem. Soc.*', 2013, **160**, (2), A306.
53. M. Ebner, D.-W. Chung, E.R. García, V. Wood, M. Ebner, D.-W. Chung, V. Wood: 'Tortuosity Anisotropy in Lithium-Ion Battery Electrodes', *Adv. Energy Mater.*', 2014, **4**, (5), n/a.
54. A. Vadakkepatt, B. Trembacki, S.R. Mathur, J.Y. Murthy: 'Bruggeman's Exponents for Effective Thermal Conductivity of Lithium-Ion Battery Electrodes', *J. Electrochem. Soc.*', 2016, **163**, (2), A119.
55. D.-W. Chung, M. Ebner, D.R. Ely, V. Wood, E.R. García: 'Validity of the Bruggeman relation for porous electrodes', *Modell. Simul. Mater. Sci. Eng.*', 2013, **21**, (7), 74009.
56. E. Ebner, F. Geldmacher, F. Marone, M. Stampanoni, V. Wood: 'X-Ray Tomography of Porous, Transition Metal Oxide Based Lithium Ion Battery Electrodes', *Adv. Energy Mater.*', 2013, **3**, (7), 845–850.
57. M. Ebner, V. Wood: 'Tool for Tortuosity Estimation in Lithium Ion Battery Porous Electrodes', *J. Electrochem. Soc.*', 2015, **162**, (2), A3064.
58. M.F. Lagadec, M. Ebner, R. Zahn, V. Wood: 'Communication—Technique for Visualization and Quantification of Lithium-Ion Battery Separator Microstructure', *J. Electrochem. Soc.*', 2016, **163**, (6), A992.
59. J. Russ, R.T. DeHoff: 'Practical Stereology, 2nd ed., Kluwer Academic/Plenum, New York, London, 2000.
60. D.E. Stephenson, E.M. Hartman, J.N. Harb, D.R. Wheeler: 'Modeling of Particle-Particle Interactions in Porous Cathodes for Lithium-Ion Batteries', *J. Electrochem. Soc.*', 2007, **154**, (12), A1146.
61. A. Gupta, J.H. Seo, X. Zhang, W. Du, A.M. Sastry, W. Shyy: 'Effective Transport Properties of LiMn2O4 Electrode via Particle-Scale Modeling', *J. Electrochem. Soc.*', 2011, **158**, (5), A487.
62. S.J. Cooper, D.S. Eastwood, J. Gelb, G. Damblanc, D.J.L. Brett, R.S. Bradley, P.J. Withers, P.D. Lee, A.J. Marquis, N.P. Brandon, P.R. Shearing: 'Image based modelling of microstructural heterogeneity in LiFePO4 electrodes for Li-ion batteries', *J. Power Sources*', 2014, **247**, 1033–1039.
63. Y. Zhang, Y. Chen, M. Yan, F. Chen: 'New formulas for the tortuosity factor of electrochemically conducting channels', *Electrochem. Commun.*', 2015, **60**, 52–55.
64. E. Wicke, R. Kallenbach: 'Die Oberflächendiffusion von Kohlendioxyd in aktiven Kohlen', *Kolloid-Zeitschrift*', 1941, **97**, (2), 135-151.
65. R.B. Evans, G.M. Watson, J. Truitt: 'Interdiffusion of Gases in a Low Permeability Graphite at Uniform Pressure', *J. Appl. Phys.*', 1962, **33**, (9), 2682–2688.
66. R.B. Evans, G.M. Watson, J. Truitt: 'Interdiffusion of Gases in a Low-Permeability Graphite. II. Influence of Pressure Gradients', *J. Appl. Phys.*', 1963, **34**, (7), 2020–2026.
67. T. Bardakci, F.G. King: 'Measurements of argon, nitrogen and carbon dioxide diffusion through random assemblies of small spheres', *Gas Sep. Purif.*', 1992, **6**, (1), 43–48.
68. R.E. Williford, L.A. Chick, G.D. Maupin, S.P. Simner, J.W. Stevenson: 'Diffusion Limitations in the Porous Anodes of SOFCs', *J. Electrochem. Soc.*', 2003, **150**, (8), A1067.
69. K. Soukup, P. Schneider, O. Šolcová: 'Comparison of Wicke–Kallenbach and Graham's diffusion cells for obtaining transport characteristics of porous solids', *Chem. Eng. Sci.*', 2008, **63**, (4), 1003–1011.

70. G. Salejova, Z. Grof, O. Solcova, P. Schneider, J. Kosek: 'Strategy for predicting effective transport properties of complex porous structures', *Computers & Chemical Engineering*', 2011, **35**, (2), 200–211.
71. G. Brus, K. Miyawaki, H. Iwai, M. Saito, H. Yoshida: 'Tortuosity of an SOFC anode estimated from saturation currents and a mass transport model in comparison with a real micro-structure', *Solid State Ionics*', 2014, **265**, 13–21.
72. W. He, J. Zou, B. Wang, S. Vilayurganapathy, M. Zhou, X. Lin, K. Zhang, J. Lin, P. Xu, J. Dickerson: 'Gas transport in porous electrodes of solid oxide fuel cells: A review on diffusion and diffusivity measurement', *J. Power Sources*', 2013, **237**, (0), 64–73.
73. E. Mason, A. Malinauskas: 'Gas transport in porous media: The dusty-gas model, Elsevier, Amsterdam, New York, 1983.
74. R.B. Bird, W.E. Stewart, E.N. Lightfoot: 'Transport phenomena, 2nd ed., J. Wiley, New York, 2002.
75. J. Yuan, B. Sundén: 'On mechanisms and models of multi-component gas diffusion in porous structures of fuel cell electrodes', *Int. J. Heat Mass Transfer*', 2014, **69**, (0), 358–374.
76. A.F. Mills: 'On steady one-dimensional diffusion in binary ideal gas mixtures', *Int. J. Heat Mass Transfer*', 2003, **46**, (13), 2495–2497.
77. A. Bertei, C. Nicolella: 'Common inconsistencies in modeling gas transport in porous electrodes: The dusty-gas model and the Fick law', *J. Power Sources*', 2015, **279**, 133–137.
78. R. Suwanwarangkul, E. Croiset, M. Fowler, P. Douglas, E. Entchev, M. Douglas: 'Performance comparison of Fick's, dusty-gas and Stefan–Maxwell models to predict the concentration overpotential of a SOFC anode', *J. Power Sources*', 2003, **122**, (1), 9–18.
79. K. Tseronis, I. Kookos, C. Theodoropoulos: 'Modelling mass transport in solid oxide fuel cell anodes: a case for a multidimensional dusty gas-based model', *Chem. Eng. Sci.*', 2008, **63**, (23), 5626–5638.
80. J.R. Izzo, A. Joshi, K. Grew, W.K.S. Chiu, A. Tkachuk, S. Wang, W. Yun: 'Non-destructive Reconstruction and Analysis of Solid Oxide Fuel Cell Anodes using X-ray Computed Tomography at sub-50 nm Resolution', *ECS Trans.*', 2008, **13**, (6), 1–11.
81. Y. Vural, L. Ma, D. Ingham, M. Pourkashanian: 'Comparison of the multicomponent mass transfer models for the prediction of the concentration overpotential for solid oxide fuel cell anodes', *J. Power Sources*', 2010, **195**, (15), 4893–4904.
82. S. Wang, W. Worek, W. Minkowycz: 'Performance comparison of the mass transfer models with internal reforming for solid oxide fuel cell anodes', *Int. J. Heat Mass Transfer*', 2012, **55**, (15-16), 3933–3945.
83. A. Bertei, B. Nucci, C. Nicolella: 'Microstructural modeling for prediction of transport properties and electrochemical performance in SOFC composite electrodes', *Chem. Eng. Sci.*', 2013, **101**, (0), 175–190.
84. B. Tjaden, J. Lane, P.J. Withers, R.S. Bradley, D.J.L. Brett, P.R. Shearing: 'The application of 3D imaging techniques, simulation and diffusion experiments to explore transport properties in porous oxygen transport membrane support materials', *Solid State Ionics*', 2016, **288**, 315–321.
85. H.V. Schmidt, C.-L. Tsai: 'Anode-pore tortuosity in solid oxide fuel cells found from gas and current flow rates', *J. Power Sources*', 2008, **180**, (1), 253–264.
86. H.V. Schmidt, C.-L. Tsai, L. Lediaev, in: Advances in Solid Oxide Fuel Cells III: Ceramic and Engineering Science Proceedings, Volume 28, Issue 4, John Wiley & Sons, Inc, 2009, pp. 127–140.
87. C.-L. Tsai, H.V. Schmidt: 'Tortuosity in anode-supported proton conductive solid oxide fuel cell found from current flow rates and dusty-gas model', *J. Power Sources*', 2011, **196**, (2), 692–699.
88. H.S. Harned, D.M. French: 'A Conductance Method For The Determination Of The Diffusion Coefficients Of Electrolytes', *Ann. N. Y. Acad. Sci.*', 1945, **46**, (5 The Diffusion), 267–284.

89. J. Newman, T.W. Chapman: 'Restricted diffusion in binary solutions', *AIChE J.*', 1973, **19**, (2), 343–348.
90. S.G. Stewart, J. Newman: 'The Use of UV/vis Absorption to Measure Diffusion Coefficients in LiPF6 Electrolytic Solutions', *J. Electrochem. Soc.*', 2008, **155**, (1), F13.
91. C.-J. Bae, C.K. Erdonmez, J.W. Halloran, Y.-M. Chiang: 'Design of Battery Electrodes with Dual-Scale Porosity to Minimize Tortuosity and Maximize Performance', *Adv. Mater.*', 2013, **25**, (9), 1254–1258.
92. M. Doyle, J. Newman: 'Analysis of capacity–rate data for lithium batteries using simplified models of the discharge process', *J. Appl. Electrochem.*', 1997, **27**, (7), 846–856.
93. P.R. Shearing, D.S. Eastwood, R.S. Bradley, J. Gelb, S.J. Cooper, F. Tariq, D.J.L. Brett, N.P. Brandon, P.J. Withers, P.D. Lee: 'Exploring electrochemical devices using X-ray microscopy: 3D microstructure of batteries and fuel cells', *Microscopy and Analysis*', 2013, **27**, (2), 19–22.
94. M. Cantoni, L. Holzer: 'Advances in 3D focused ion beam tomography', *MRS Bull.*', 2014, **39**, (04), 354–360.
95. E. Maire, P.J. Withers: 'Quantitative X-ray tomography', *Int. Mater. Rev.*', 2014, **59**, (1), 1–43.
96. G.J. Nelson, W.M. Harris, J.J. Lombardo, J.R. Izzo, W.K.S. Chiu, P. Tanasini, M. Cantoni, J. van Herle, C. Comninellis, J. Andrews, Y. Liu, P. Pianetta, Y. Chu: 'Comparison of X-ray Nanotomography and FIB-SEM in Quantifying the Composite LSM/YSZ SOFC Cathode Microstructure', *ECS Trans.*', 2011, **35**, (1), 2417–2421.
97. P.R. Shearing, J. Gelb, N.P. Brandon: 'Characterization of SOFC Electrode Microstructure Using Nano-Scale X-ray Computed Tomography and Focused Ion Beam Techniques: a Comparative Study', *ECS Trans.*', 2009, **19**, (17), 51–57.
98. J. Wilson, W. Kobsiriphat, R. Mendoza, H. Chen, J. Hiller, D. Miller, K. Thornton, P. Voorhees, S. Adler, S. Barnett: 'Three-dimensional reconstruction of a solid-oxide fuel-cell anode', *Nat. Mater.*', 2006, **5**, (7), 541–544.
99. H. Iwai, N. Shikazono, T. Matsui, H. Teshima, M. Kishimoto, R. Kishida, D. Hayashi, K. Matsuzaki, D. Kanno, M. Saito, H. Muroyama, K. Eguchi, N. Kasagi, H. Yoshida: 'Quantification of SOFC anode microstructure based on dual beam FIB-SEM technique', *J. Power Sources*', 2010, **195**, (4), 955–961.
100. Y. Chen-Wiegart, S. Cronin, Q. Yuan, K. Yakal-Kremski, S. Barnett, J. Wang: '3D Non-destructive morphological analysis of a solid oxide fuel cell anode using full-field X-ray nano-tomography', *J. Power Sources*', 2012, **218**, (0), 348–351.
101. N. Vivet, S. Chupin, E. Estrade, A. Richard, S. Bonnamy, D. Rochais, E. Bruneton: 'Effect of Ni content in SOFC Ni-YSZ cermets: A three-dimensional study by FIB-SEM tomography', *J. Power Sources*', 2011, **196**, (23), 9989–9997.
102. P.R. Shearing, N.P. Brandon, J. Gelb, R.S. Bradley, P.J. Withers, A.J. Marquis, S.J. Cooper, S.J. Harris: 'Multi Length Scale Microstructural Investigations of a Commercially Available Li-Ion Battery Electrode', *J. Electrochem. Soc.*', 2012, **159**, (7), A1023.
103. J.M. Zalc, S.C. Reyes, E. Iglesia: 'The effects of diffusion mechanism and void structure on transport rates and tortuosity factors in complex porous structures', *Chem. Eng. Sci.*', 2004, **59**, (14), 2947–2960.
104. Y. Zhang, C. Xia, M. Ni: 'Simulation of sintering kinetics and microstructure evolution of composite solid oxide fuel cells electrodes', *Int. J. Hydrogen Energy*', 2012, **37**, (4), 3392–3402.
105. D. Gostovic, J.R. Smith, D. Kundinger, K.S. Jones, E.D. Wachsman: 'Three-Dimensional Reconstruction of Porous LSCF Cathodes', *Electrochem. Solid-State Lett.*', 2007, **10**, (12), B214.
106. J.R. Smith, A. Chen, D. Gostovic, D. Hickey, D. Kundinger, K.L. Duncan, R.T. DeHoff, K.S. Jones, E.D. Wachsman: 'Evaluation of the relationship between cathode microstructure and electrochemical behavior for SOFCs', *Solid State Ionics*', 2009, **180**, (1), 90–98.

107. S.J. Cooper, M. Kishimoto, F. Tariq, R.S. Bradley, A.J. Marquis, N.P. Brandon, J.A. Kilner, P.R. Shearing: 'Microstructural Analysis of an LSCF Cathode Using In Situ Tomography and Simulation', *ECS Trans.*', 2013, **57**, (1), 2671–2678.
108. P.S. Jørgensen, K.V. Hansen, R. Larsen, J.R. Bowen: 'Geometrical characterization of interconnected phase networks in three dimensions', *J. Microsc.*', 2011, **244**, (1), 45–58.
109. P.S. Jørgensen, S.L. Ebbehøj, A. Hauch: 'Triple phase boundary specific pathway analysis for quantitative characterization of solid oxide cell electrode microstructure', *J. Power Sources*', 2015, **279**, 686–693.
110. Y. Chen-Wiegart, R. DeMike, C. Erdonmez, K. Thornton, S. Barnett, J. Wang: 'Tortuosity Characterization of 3D Microstructure at Nano-scale for Energy Storage and Conversion Materials', *J. Power Sources*', 2014, **249**, (0), 349–356.
111. P.R. Shearing, L.E. Howard, P.S. Jørgensen, N.P. Brandon, S.J. Harris: 'Characterization of the 3-dimensional microstructure of a graphite negative electrode from a Li-ion battery', *Electrochem. Commun.*', 2010, **12**, (3), 374–377.
112. A. Çeçen, E.A. Wargo, A.C. Hanna, D.M. Turner, S.R. Kalidindi, E.C. Kumbur: '3-D Microstructure Analysis of Fuel Cell Materials: Spatial Distributions of Tortuosity, Void Size and Diffusivity', *J. Electrochem. Soc.*', 2012, **159**, (3), B299.
113. P.R. Shearing, R.S. Bradley, J. Gelb, S. Lee, A. Atkinson, P.J. Withers, N.P. Brandon: 'Using Synchrotron X-Ray Nano-CT to Characterize SOFC Electrode Microstructures in Three-Dimensions at Operating Temperature', *Electrochem. Solid-State Lett.*', 2011, **14**, (10), B117.
114. S.J. Cooper: 'Quantifying the Transport Properties of Solid Oxide Fuel Cell Electrodes. Ph.D. Thesis, London, 2015.
115. A.S. Joshi, K.N. Grew, J.R. Izzo, A.A. Peracchio, W.K.S. Chiu: 'Lattice Boltzmann Modeling of Three-Dimensional, Multicomponent Mass Diffusion in a Solid Oxide Fuel Cell Anode', *J. Fuel Cell Sci. Technol.*', 2010, **7**, (1), 11006.
116. K.N. Grew, Y.S. Chu, J. Yi, A.A. Peracchio, J.R. Izzo, Y. Hwu, F. de Carlo, W.K.S. Chiu: 'Nondestructive Nanoscale 3D Elemental Mapping and Analysis of a Solid Oxide Fuel Cell Anode', *J. Electrochem. Soc.*', 2010, **157**, (6), B783.
117. K.N. Grew, A.A. Peracchio, A.S. Joshi, J.R. Izzo, W.K.S. Chiu: 'Characterization and analysis methods for the examination of the heterogeneous solid oxide fuel cell electrode microstructure. Part 1: Volumetric measurements of the heterogeneous structure', *J. Power Sources*', 2010, **195**, (24), 7930–7942.
118. S.J. Cooper: 'TauFactor: MatLab App for calculating the tortuosity factor of microstructure, 2015, available online: https://sourceforge.net/projects/taufactor/, accessed 16 May 2016.
119. M.C. Sukop, D.T. Thorne: 'Lattice Boltzmann modeling: An introduction for geoscientists and engineers, Springer, Berlin, New York, 2006.
120. L. Hao, P. Cheng: 'Lattice Boltzmann simulations of anisotropic permeabilities in carbon paper gas diffusion layers', *J. Power Sources*', 2009, **186**, (1), 104–114.
121. D. Kanno, N. Shikazono, N. Takagi, K. Matsuzaki, N. Kasagi: 'Evaluation of SOFC anode polarization simulation using three-dimensional microstructures reconstructed by FIB tomography', *Electrochim. Acta*', 2011, **56**, (11), 4015–4021.
122. K. Matsuzaki, N. Shikazono, N. Kasagi: 'Three-dimensional numerical analysis of mixed ionic and electronic conducting cathode reconstructed by focused ion beam scanning electron microscope', *J. Power Sources*', 2011, **196**, (6), 3073–3082.
123. T. Shimura, Z. Jiao, S. Hara, N. Shikazono: 'Quantitative analysis of solid oxide fuel cell anode microstructure change during redox cycles', *J. Power Sources*', 2014, **267**, 58–68.
124. A. Nabovati, J. Hinebaugh, A. Bazylak, C.H. Amon: 'Effect of porosity heterogeneity on the permeability and tortuosity of gas diffusion layers in polymer electrolyte membrane fuel cells', *J. Power Sources*', 2014, **248**, 83–90.

125. M. Espinoza, B. Sundén, M. Andersson, J. Yuan: 'Analysis of Porosity and Tortuosity in a 2D Selected Region of Solid Oxide Fuel Cell Cathode Using the Lattice Boltzmann Method', *ECS Trans.*', 2015, **65**, (1), 59–73.
126. A.S. Joshi, A.A. Peracchio, K.N. Grew, W.K.S. Chiu: 'Lattice Boltzmann method for multi-component, non-continuum mass diffusion', *J. Phys. D: Appl. Phys.*', 2007, **40**, (23), 7593–7600.
127. N. Vivet, S. Chupin, E. Estrade, T. Piquero, P.L. Pommier, D. Rochais, E. Bruneton: '3D Microstructural characterization of a solid oxide fuel cell anode reconstructed by focused ion beam tomography', *J. Power Sources*', 2011, **196**, (18), 7541–7549.
128. M. Kishimoto, H. Iwai, M. Saito, H. Yoshida: 'Quantitative Evaluation of Transport Properties of SOFC Porous Anode by Random Walk Process', *ECS Trans.*', 2009, **25**, (2), 1887–1896.
129. M. Kishimoto, H. Iwai, M. Saito, H. Yoshida: 'Quantitative evaluation of solid oxide fuel cell porous anode microstructure based on focused ion beam and scanning electron microscope technique and prediction of anode overpotentials', *J. Power Sources*', 2011, **196**, (10), 4555–4563.
130. M. Kishimoto, H. Iwai, K. Miyawaki, M. Saito, H. Yoshida: 'Improvement of the sub-grid-scale model designed for 3D numerical simulation of solid oxide fuel cell electrodes using an adaptive power index', *J. Power Sources*', 2013, **223**, 268–276.
131. F. Tariq, V. Yufit, M. Kishimoto, P.R. Shearing, S. Menkin, D. Golodnitsky, J. Gelb, E. Peled, N.P. Brandon: 'Three-dimensional high resolution X-ray imaging and quantification of lithium ion battery mesocarbon microbead anodes', *J. Power Sources*', 2014, **248**, 1014–1020.
132. P.P. Mitra, P.N. Sen, L.M. Schwartz, P. Le Doussal: 'Diffusion propagator as a probe of the structure of porous media', *Phys. Rev. Lett.*', 1992, **68**, (24), 3555–3558.
133. P.P. Mitra, P.N. Sen, L.M. Schwartz: 'Short-time behavior of the diffusion coefficient as a geometrical probe of porous media', *Phys. Rev. B*', 1993, **47**, (14), 8565–8574.
134. Y. Nakashima, S. Kamiya: 'Mathematica Programs for the Analysis of Three-Dimensional Pore Connectivity and Anisotropic Tortuosity of Porous Rocks using X-ray Computed Tomography Image Data', *J. Nucl. Sci. Technol.*', 2007, **44**, (9), 1233–1247.
135. M. Kishimoto, H. Iwai, M. Saito, H. Yoshida: 'Three-Dimensional Simulation of SOFC Anode Polarization Characteristics Based on Sub-Grid Scale Modeling of Microstructure', *J. Electrochem. Soc.*', 2012, **159**, (3), B315.
136. B. Rüger, A. Weber, E. Ivers-Tiffee: '3D-Modelling and Performance Evaluation of Mixed Conducting (MIEC) Cathodes', *ECS Trans.*', 2007, **7**, (1), 2065–2074.
137. B. Rüger, J. Joos, A. Weber, T. Carraro, E. Ivers-Tiffée: '3D Electrode Microstructure Reconstruction and Modelling', *ECS Trans.*', 2009, **25**, (2), 1211–1220.
138. J. Joos, T. Carraro, A. Weber, E. Ivers-Tiffée: 'Reconstruction of porous electrodes by FIB/SEM for detailed microstructure modeling', *J. Power Sources*', 2011, **196**, (17), 7302–7307.
139. A. Häffelin, J. Joos, M. Ender, A. Weber, E. Ivers-Tiffée: 'Time-Dependent 3D Impedance Model of Mixed-Conducting Solid Oxide Fuel Cell Cathodes', *J. Electrochem. Soc.*', 2013, **160**, (8), F867.
140. M. Ender, J. Joos, T. Carraro, E. Ivers-Tiffée: 'Three-dimensional reconstruction of a composite cathode for lithium-ion cells', *Electrochem. Commun.*', 2011, **13**, (2), 166–168.
141. J. Joos, M. Ender, T. Carraro, A. Weber, E. Ivers-Tiffée: 'Representative volume element size for accurate solid oxide fuel cell cathode reconstructions from focused ion beam tomography data', *Electrochim. Acta*', 2012, **82**, 268–276.
142. S. Cronin, J. Wilson, S. Barnett: 'Impact of pore microstructure evolution on polarization resistance of Ni-Yttria-stabilized zirconia fuel cell anodes', *J. Power Sources*', 2011, **196**, (5), 2640–2643.
143. A. Nanjundappa, A.S. Alavijeh, M. El Hannach, D. Harvey, E. Kjeang: 'A customized framework for 3-D morphological characterization of microporous layers', *Electrochim. Acta*', 2013, **110**, 349–357.

144. J. Laurencin, R. Quey, G. Delette, H. Suhonen, P. Cloetens, P. Bleuet: 'Characterisation of Solid Oxide Fuel Cell Ni–8YSZ substrate by synchrotron X-ray nano-tomography: from 3D reconstruction to microstructure quantification', *J. Power Sources*', 2012, **198**, 182–189.
145. B. Vijayaraghavan, E. Garcia, Y.-M. Chiang: 'Microstructure Modeling of Rechargeable Lithium-Ion Batteries', *Meeting Abstracts*', 2011, **MA2011-01**, (10), 502.
146. P. Trogadas, O.O. Taiwo, B. Tjaden, T.P. Neville, S. Yun, J. Parrondo, V. Ramani, M.-C. Coppens, D.J.L. Brett, P.R. Shearing: 'X-ray micro-tomography as a diagnostic tool for the electrode degradation in vanadium redox flow batteries', *Electrochem. Commun.*', 2014, **48**, (0), 155–159.
147. A.G. Kashkooli, S. Farhad, D.U. Lee, K. Feng, S. Litster, S.K. Babu, L. Zhu, Z. Chen: 'Multiscale modeling of lithium-ion battery electrodes based on nano-scale X-ray computed tomography', *J. Power Sources*', 2016, **307**, 496–509.
148. S.J. Harris, P. Lu: 'Effects of Inhomogeneities—Nanoscale to Mesoscale—on the Durability of Li-Ion Batteries', *J. Phys. Chem. C*', 2013, **117**, (13), 6481–6492.
149. B. Mandelbrot: 'How Long Is the Coast of Britain? Statistical Self-Similarity and Fractional Dimension', *Science*', 1967, **156**, (3775), 636–638.
150. M.S. Costanza-Robinson, B.D. Estabrook, D.F. Fouhey: 'Representative elementary volume estimation for porosity, moisture saturation, and air-water interfacial areas in unsaturated porous media: Data quality implications', *Water Resour. Res.*', 2011, **47**, (7), W07513.
151. I. Robertson, L. Holzer, M. Prestat, B. Münch, T. Graule: 'Effects of particle and pore sizes, surface area and porosity on the performance of LSC cathodes', *Proceedings of the 9th European Fuel Cell Forum*', 2010, 10–83.